2011

Synaptic Contact Localization in Three Dimensional Space Using a Center Distance Algorithm

Benjamin D. Ausdenmoore
Wright State University

SYNAPTIC CONTACT LOCALIZATION IN THREE DIMENSIONAL SPACE USING A CENTER DISTANCE ALGORITHM

A thesis submitted in partial fulfillment
of the requirements for the degree of
Master of Science

By

BENJAMIN DAVID AUSDENMOORE
B.S., Wright State University, 2008

2011
Wright State University

WRIGHT STATE UNIVERSITY

SCHOOL OF GRADUATE STUDIES

November 7, 2011

I HEREBY RECOMMEND THAT THE THESIS PREPARED UNDER MY SUPERVISION BY Benjamin David Ausdenmoore ENTITLED Synaptic Contact Localization in Three Dimensional Space Using a Center Distance Algorithm BE ACCEPTED IN PARTIAL FULFILMENT OF THE REQUIREMENTS FOR THE DEGREE OF Master of Science

_____

David R. Ladle, Ph.D.
Thesis Director

_____

Timothy C. Cope, Ph.D.
Chair, Department of
Neuroscience, Cell Biology
and Physiology
College of Science and
Mathematics

Committee of
Final Thesis

_____

David R. Ladle, Ph.D.

_____

Mark M. Rich, M.D. Ph.D.

_____

Christopher N. Wyatt, Ph.D.

_____

Andrew Hsu, Ph.D.
Dean, School of Graduate Studies

Abstract

Ausdenmoore, Benjamin David. M.S., Department of Neuroscience, Cell Biology and Physiology, Wright State University, 2011. Synaptic Contact Localization in Three Dimensional Space Using a Center Distance Algorithm.

Spatial distribution of synaptic inputs on the dendritic tree of a neuron can have significant influence on neuronal function. Consequently, accurate anatomical reconstructions of neuron morphology and synaptic localization are critical when modeling and predicting physiological responses of individual neurons. Historically, generation of three-dimensional (3D) neuronal reconstructions together with comprehensive mapping of synaptic inputs has been an extensive task requiring manual identification of putative synaptic contacts directly from tissue samples or digital images. Recent developments in neuronal tracing software applications have improved the speed and accuracy of 3D reconstructions, but localization of synaptic sites through the use of pre- and/or post-synaptic markers has remained largely a manual process. To address this, we developed an algorithm, based on 3D distance measurements between putative pre-synaptic terminals and the post-synaptic dendrite. The algorithm is implemented with custom Matlab routines, and its effectiveness evaluated through analysis of primary sensory afferent terminals on motor neurons.

TABLE OF CONTENTS

FIGURES

TABLES

I would like to preface the following thesis with a note that much of the core algorithm and initial results have been published in the Journal of Neuroscience Methods. The article is titled *"Localization of presynaptic inputs on dendrites of individually labeled neurons in three dimensional space using a center distance algorithm."*

Currently the source code is not published in its entirety. However, in the appendix you will be able to find the pseudo code representation of it. It was coded in the Matlab environment. Further questions in regard to the program and any of the results should be directed to Dr. David Ladle at David(dot)Ladle(at)wright(dot)edu or to Benjamin Ausdenmoore at Ausdenmoore(dot)3(at)wright(dot)edu.

Acknowledgements

Without the continued support from my advisor and mentor, Dr. David Ladle, this project never would have come to fruition. His guidance and patience over the past few years have also helped mold me into the scientist that I am today and for this I thank him.

I also owe a hearty thanks to Drs. Timothy Cope, Robert Putnam, Jason Deibel and Michael Hennessy. These gentlemen helped me realize that the current path I was traveling wasn't necessarily the best one for me at the time and essentially gave me a chance to see that for myself.

To Diane Ponder, Dr. Gerald Alter, Karen Luchin, Dr. Larry Ream and Kim Hagler. I greatly appreciate the student centered mindset all of you have demonstrated over the years. The graduate programs you oversee, or oversaw at the time, would not be where they are today without the efforts of each and every one of you.

I would like to thank Dr. Valarie Neff, Jackie Sisco and Zack Markwell for their assistance with the manual analysis for the images used in this project. In addition I'd also like to thank Zach for his help in debugging the code during the testing period.

Finally I would like to thank my friends and family. Without you there wouldn't be a shred of sanity left in this mind of mine. All of you reminded me that there needs to be time taken to relax and let things go, especially after countless hours of analysis or unsuccessful experiments.

For mom and dad…

Chapter 1: Introduction

Neurons in different parts of the brain exhibit significant variation in morphology, including the extent and complexity of the dendritic arbor. Fundamental engineering principles have been applied in an effort to explain this variability in biological morphology. Essentially, neurons must balance the cost associated with developing the membrane necessary to create the dendritic arbors with the need for a sufficient dendritic arbor to maximize the number of contacts they can make with incoming axons (Wen & Chklovskii, 2008). For example, purkinje cells receive inputs from parallel fibers in the cerebellum, and these parallel fibers project axons primarily in one direction. The purkinje cells use this to their advantage and develop elaborate dendrites in a planar array perpendicular to the projection of the parallel fibers. This pattern is in contrast to the orientation of incoming axons that the pyramidal cells receive connections from in the cerebrum. Incoming axons in this region of the brain are far less ordered in terms of their orientation and in order to maximize the connections the pyramidal cell can make their dendrites project in a seemingly random fashion.

The spatial distribution of synaptic inputs along the dendritic tree can have significant effects on neuronal function, and is critical to understand how neurons process information individually and in circuits (Hausser and Mel, 2003). A study of the descending inputs from the vestibulospinal tract (VST) onto motor neurons innervating the splenius muscle, an important neck muscle, showed that most of the connections

being made were in the medial dendrites of these motor neurons (Grande et al., 2005). VST synapses are thought to be a fairly weak synapse (Grande et al., 2005; Fyffe, 2001) but physiologically the response was much greater due to this organization. Furthermore, when these cells were modeled and the VST terminations placed evenly throughout the motor neuron dendrites the resulting output was greatly diminished with respect to original physiological measurements (Grande et al., 2010). Nevertheless, creating morphological reconstructions with comprehensive maps of synaptic contact locations has been a significant, time-consuming, and largely manual task which can yield large amounts of information.

Early efforts identified putative sites of synaptic contact by labeling single pre- and post-synaptic neurons with horseradish peroxidase (HRP) (Brown and Fyffe, 1981; Redman and Walmsley, 1983). Locations of synaptic contacts were visually determined at high magnification as close appositions of the labeled axon and dendrite. Reconstructions of the post-synaptic neuron were made manually using a camera lucida attachment. This strategy was limited, however, in that only a small fraction of the total synaptic contacts on a given post-synaptic neuron could be identified.

Increasingly detailed molecular characterization of synaptic proteins has allowed discrimination by immunohistochemistry of multiple synaptic types. Synaptic sites can then be inferred from discrete concentrations of pre- and post-synaptic proteins using light microscopy. Post-synaptic indicators of synaptic contacts include neurotransmitter receptors and proteins of the post-synaptic density. Gephyrin, for example, is associated with glycine and $GABA_A$ receptor clusters at inhibitory synaptic sites (Essrich et al., 1998; Kirsch et al., 1993), while PSD-95 associates with glutamate receptors at excitatory

synapses (Cho et al., 1992; Marrs et al., 2001). Similarly, pre-synaptic terminals of neurons that employ different neurotransmitters can be identified by accumulations of pre-synaptic associated proteins. Direct input from serotonergic neurons can be visualized through immunoreactivity against the neurotransmitter serotonin itself, which is concentrated in terminal boutons (Alvarez et al., 1998). Proteins involved in the synthesis of neurotransmitters can also be useful in identifying synaptic terminals of particular modalities. For example, isoforms of glutamic acid decarboxylase (GAD65 and GAD67) mark terminal boutons arising from subpopulations of GABA-ergic interneurons in the spinal cord (Mackie et al., 2003). Lastly, proteins required for neurotransmitter loading into synaptic vesicles, such as isoforms of vesicular glutamate transporters (VGLUT1, VGLUT2), are highly concentrated in terminal boutons (Alvarez et al., 2004; Todd et al., 2003).

Identification of particular types of synaptic inputs on neurons of interest can assist in mapping connections within neural circuits and this approach has yielded significant results in studies of pre-motor synaptic inputs to motor neurons in the mammalian spinal cord. Prior to the rise of immunohistochemical identification of synaptic terminal types, synaptic boutons on motor neurons were divided into several groups on the basis of similarity at the ultrastructural level (Conradi and Skoglund, 1969). The cellular origins of many of these boutons have now been defined through immunohistochemical approaches. For example, synaptic terminals originally identified as S-boutons are now known to arise from glutamatergic primary sensory afferents which utilize VGLUT1 to load glutamate (Alvarez et al., 2004; Conradi et al., 1983; Todd et al., 2003). In contrast, glutamatergic spinal interneuron terminals are enriched for VGLUT2,

thus allowing for differentiation of these two synaptic inputs to motor neurons (Alvarez et al., 2004; Todd et al., 2003). Large cholinergic terminals called C-boutons have recently been shown to be derived from a population of interneurons located close to the central canal (Miles et al., 2007; Zagoraiou et al., 2009). Motor neurons also receive recurrent inhibition from Renshaw cells; these inhibitory terminals express high levels of the calcium buffering protein, calbindin (Alvarez and Fyffe, 2007). Thus, the possibility exists for the generation of detailed maps of synaptic contacts originating from multiple sources on digital reconstructions of individual neurons.

Creating a map of contacts from a specific type of synaptic input to an individual neuron can also provide insight into neuronal function. In retinal ganglion cells, for example, the density of both glycine and $GABA_A$ receptor clusters are more than 10-fold higher in distal regions of the dendritic tree than in proximal regions (Lin et al., 2000). In contrast, glutamate receptors and associated post-synaptic density proteins are uniformly distributed across the dendritic arbor (Jakobs et al., 2008; Lin et al., 2002). In addition, excitatory synapses are found in regularly spaced intervals along dendrites of different types of retinal ganglion cells (Koizumi et al., 2011). Such studies require large amounts manual analysis to complete. Improvements in the efficiency with which these maps can be created will allow circuit analysis in greater detail, and make comparisons of connectivity among different cell types a practical possibility.

Recent advances in automatic and semi-automatic algorithms promise to reduce both the time and effort required for accurate reconstructions of neuronal structures (Meijering, 2010). For example, NeuronJ, a Java-based software plug-in for the ImageJ analysis package, automatically detects neurite pathways in two-dimensional images

from starting locations provided by user input and also allows users to correct traced paths (Meijering et al., 2004). New algorithms for delineating neuronal structures from fluorescence imaging stacks in three dimensions (3D) have also been proposed (Evers et al., 2005; Rodriguez et al., 2006, 2009; Schmitt et al., 2004; Vasilkoski and Stepanyants, 2009; Wearne et al., 2005). Some of these techniques are freely available for individual adaptation but each has its own combination of benefits and limitations.

Evers et al. (2005) provide a semi-automated algorithm that only requires the user to define points of branching. Once the branch points are determined the algorithm will then determine the midline and cylindrical structure of the dendrites. A major limitation of this algorithm is also what provides for the expedience of it, the use of the TEASAR algorithm (Sato et al., 2000). TEASAR requires the use of hierarchical data to prevent the occurrence of loops that could form in the skeletonization stage and in the event that a circular loop should form the algorithm will fail to execute fully. The skeletonization stage is necessary to take the initial volumetric data to a single line representing the path of the object, analogous to the human skeleton beneath our layers of tissue. Additionally, upon attempting to convert the entire process to an automatic one the occurrence of small proliferative branches, which impair the ability to estimate the radial measurements, began to occur which became extremely time consuming to deal with.

Wearne et al. (2005) employed a rayburst sampling algorithm that differs from Evers strategy in the fact that it doesn't require a midline to make measurements from yet can still return the dendritic diameter. This is achieved by measuring the length of multiple rays sent in various directions out from the current point. The length of these rays, number of voxels in length, is then sorted and the value that sits at the 25^{th}

percentile is the value used for the diameter measurement for the current point. Using the 25^{th} percentile as the measurement provides good resistance against local irregularities in the surface and does not depend on the orientation of the segment (Rodriguez et al., 2003). In addition the rayburst algorithm can be used to measure dendritic surface area and volume and their approach allows for output of the data in a .swc format commonly used for neuroanatomical modeling with a program like Neuron Studio (Cannon et al., 1998).

Rodriquez et al. (2009) have developed a voxel scooping method that simply requires a single seed point to develop the centerline of the dendritic structure in question, even with the soma being present. This is achieved by developing layers of increasing valued voxels within the structure you're analyzing, the values increase in an outward radial direction from the seed point. The first node is positioned at the seed point and then scoops the voxels within the scooping distance defined by the user. A new node is then placed halfway between the computed center of mass of the scooped voxels and the current parent node. This new node now becomes the parent and the process continues until the entire structure is traced. This algorithm (Rodriguez et al., 2009) boasts a great run speed but only yields the centerline of the dendrite without any subsequent information. Additional information becomes necessary to estimate the volume of the dendrite, the radius or to provide enough data to adequately model the dendrite in the future.

Schmitt et al. (2004) delivered a program that is usable across multiple computer platforms. This program provides an accelerated process that generates very accurate results by utilizing automatic fitting. The automatic fitting is the result of using a

mathematical snake and geodesic active contours which provides for an evolving curve fit to the geometric shape based upon measures of the curve contours and calculation of the path that requires the least amount of energy to follow, essentially the tightest fit to the object of interest. Ultimately, this provides for detection of the 3D boundaries of the object and the information can then be used to generate weighted curves that will be used to fit the centerline. The major unique aspect of this program is the ability of it to provide a surface of the dendrite in addition to the centerline.

Automating the process of mapping synaptic contacts or clusters of particular proteins on traced dendrites has received less attention. Two recent approaches have worked to improve the efficiency of this process through spatial correlation of signals in a second channel representing synaptic or other subcellular structures with neural structures defined by an automatic neuronal tracing method. Evers and colleagues mapped the fluorescent intensity of pre- and/or post-synaptic protein markers onto a 3D isosurface representing a traced dendrite (Evers et al., 2005). In this strategy, only those voxels within a user-defined distance from the surface are analyzed as possible synaptic contacts. Putative synaptic locations are then identified from local concentrations of these markers. Ballou and colleagues measured clusters of $CaV_{1.3}$, a channel involved in modulating properties of active dendrites, along the 3D path of traced dendrites (Ballou et al., 2006). In this case, only $CaV_{1.3}$ signal located within a 3D mask generated from the neuronal dendrite was considered, in order to eliminate confounding results from $CaV_{1.3}$ located outside of the labeled dendrites.

Here we present a semi-automated, graphical user interface (GUI) driven algorithm, implemented in Matlab, for detection of synaptic contacts on labeled dendrites

in 3D digital image stacks. This method facilitates construction of a 3D spatial map of synaptic inputs onto the dendritic tree of a single neuron. User input is required only while pre-processing the data channels to ensure separation of signals of interest from background, and to determine start and stop locations for tracing the dendrite to be analyzed. Putative synaptic contact detection then proceeds automatically, utilizing predefined objective criteria for contact detection. We compare the efficiency of this algorithm with manual contact identification and find similar contact detection rates. Substantial time savings and the elimination of discrepancies in contact detection introduced by different users are significant advantages of this method. In addition the program provides sufficient output that additional analysis can be done outside of the program, visualized in Imaris and/or modeled in a program like Neuron Studio.

Chapter 2: Materials and Methods

2.1. Tissue preparation and immunohistochemistry

2.1.1. Intracellular fluorescent labeling of individual motor neurons

The images used to test the center distance algorithm data were obtained from individual motor neurons labeled with neurobiotin. This existing data set was not generated as a part of this thesis work, but a brief description of the relevant methods is presented here. Motor neurons were injected with neurobiotin during sharp-electrode intracellular recordings in isolated spinal cord preparations from 7 day-old C57Bl/6J mice. All animal procedures were approved by the Laboratory Animal Care and Use Committee at Wright State University. Detailed methods regarding dissection of the spinal cord and recording conditions have been published previously (Mears and Frank, 1997). High resistance (75 to 110 MΩ) electrodes were filled with 5% (w:v) neurobiotin in 1M KAc. Fast Green (Sigma, St. Louis) was also added to aid visualization of the electrode tip (0.15% final concentration [w:v]). General positioning of the electrode tip before penetration of the spinal cord was performed using a stereo dissecting microscope (Olympus SZX16), but motor neurons were impaled blindly. Motor neurons were identified by the presence of an antidromic action potential following stimulation of motor axons in the ventral root. Neurobiotin was injected by positive current pulses (1.0 – 2.0nA) for 10 to 20 minutes (300ms pulses at 1.0Hz). The preparation was then left undisturbed for 45 minutes to one hour to ensure distribution of neurobiotin throughout

the dendritic tree. The spinal cord was fixed in ice-cold 4% paraformaldehyde (Sigma, St. Louis) for two hours, then cryoprotected (30% sucrose in PBS), frozen on dry ice, and cut in the transverse plane (50µm thick sections) using a cryostat.

Immunohistochemistry procedures were carried out on free-floating sections. Neurobiotin was visualized with streptavidin Alexa-488 (Invitrogen; 1:1000 dilution). Synaptic terminals of primary sensory afferents were revealed by staining for VGLUT1 (guinea pig anti VGLUT1, Chemicon; 1:10,000 dilution) using a Cy3-conjugated secondary antibody (donkey anti guinea pig Cy3, Jackson ImmunoResearch).

2.1.2. Bulk fluorescent labeling of motor neurons

To test additional features of the center distance algorithm, such as addressing tissue shrinkage during immunohistochemistry, in vitro experiments were performed to fluorescently label multiple motor neurons by retrograde transport through the ventral root. As these experiments were performed as part of this thesis project, detailed methods are presented here. Motor neurons were labeled using a partial root backfill on the L4 ventral root of a 7 day-old C57Bl/6J mouse spinal cord in accordance with animal procedures approved by the Laboratory Animal Care and Use Committee at Wright State University. The spinal cord was removed by performing a dorsal laminectomy followed by removal of the remaining vertebral bones in the lumbar region while the tissue was in a cold recirculating bath of artificial cerebrospinal fluid (ACSF) (Mears and Frank 1997). A glass capillary tube (1B120F-4, World Precision Instruments Inc.) was fire polished to develop a small tip that was roughly 1/3 of the diameter of the nerve root. The electrode tip was placed in close proximity to the ventral root using a micromanipulator and

negative pressure was applied to suck up a portion of the root into the capillary. ACSF was evacuated from the electrode using a micropipette and 3µl of 3000MW tetramethylrhodamine conjugated dextran (Invitrogen #D3308, 10mg/ml) was loaded into the electrode. The preparation was allowed to sit for five hours at room temperature to allow for sufficient labeling of the motor neurons to occur. The spinal cord was then fixed in ice-cold 4% paraformaldehyde (Sigma, St. Louis) for two hours, cryoprotected (30% sucrose in PBS) overnight, frozen in tissue freezing medium (Cat. # 72592, Electron Microscopy Sciences), and cut in the transverse plane (50µm thick sections) using a cryostat.

Immunohistochemistry procedures were carried out on free-floating sections. Rhodamine was visualized with a rabbit anti-Rhodamine (Invitrogen; 1:1000 dilution) primary antibody followed with a Cy3 conjugated secondary antibody (donkey anti rabbit Cy3, Jackson ImmunoResearch; 1:1000 dilution). Synaptic terminals of primary sensory afferents were revealed by staining for VGLUT1 (guinea pig anti VGLUT1, Chemicon; 1:10,000 dilution) paired with an Alex488-conjugated secondary antibody (goat anti guinea pig Alex488, Invitrogen; 1:1000 dilution).

2.2. Image data acquisition

Images were obtained on a confocal microscope (Olympus FV1000) at high magnification (Olympus UPLSAPO 60X oil-immersion objective, 1.35 N.A., 2.5X scan zoom) to provide adequate spatial sampling frequency for subsequent image deconvolution (0.086µm XY pixel size and 0.21µm optical section thickness). Laser excitation wavelengths for Alexa-488 and Cy3 were 488nm (argon laser) and 568nm

(krypton laser), respectively. Emitted photons were detected using band pass filters (Alexa-488, 500-555nm; Cy3, 580-680nm). Channels were scanned sequentially and a 2X Kalman filter was used to reduce background signal. The use of the super apochromatic objective lens minimized effects of chromatic aberration. To minimize scanning time, pixel dwell time was reduced to the shortest possible duration (2.0µsec). The time required to scan an optical section for both channels at full 1024 X 1024 pixel image size was 13 seconds, and scanning 100 optical sections (representing a tissue thickness of approximately 21µm) required 22 minutes. In practice, however, the region to be scanned was routinely cropped to include only the dendrite of interest to minimize scanning time. Laser intensities were limited to < 5% of maximum transmission levels to reduce photobleaching. Resulting 3D data sets were deconvolved with a theoretical point-spread function using Huygens Pro (SVI, Hilversum, The Netherlands). A sample image is shown in Figure 1A.

Images used for the Z-axis shrinkage experiment were gathered using the same imaging protocols stated above with the following adaptation. High magnification scans were made at slighter lower resolution (0.08µm XY pixel size and 0.3µm optical section thickness) to reduce scan time as deconvolution was not necessary. Scans were performed the same day the tissue was placed on the slide and cover-slipped. Subsequent scans were taken 7, 14 and 28 days post cover-slipping to allow for potential tissue shrinkage to be measured. A low magnification image was taken using a 20X objective for reference so similar images could be taken at 60x in the additional sessions.

2.3. Manual image analysis and contact determination

All data sets were first analyzed using Neurolucida (version 9.0, MBF, Williston, VT) by four independent users. Requirements for synaptic contact detection followed published criteria (Alvarez et al., 1998; Brown and Fyffe, 1981; Fyffe, 1991; Grande et al., 2005; Grande et al., 2010; Rose et al., 1995). Users could examine each optical section in the XY plane. The presence of yellow voxels resulting from overlap of both VGLUT1 (red) and neurobiotin dendrite (green) signals in at least one optical section were required for a VGLUT1 terminal to be ruled as a synaptic contact. Even if a VGLUT1 terminal was located adjacent to the dendrite, it was not counted as a synaptic contact if no yellow pixels could be discerned by the user.

Some variability among users was noted in the placement of synaptic markers, but discrepancies were usually less than 5 pixels in the XY plane (or about 0.45μm). In order to determine if synaptic markers placed by multiple users referred to the same VGLUT1 object, the location of user identified contacts was compared to the set of VGLUT1 objects defined during image pre-processing steps (described in section 3.1). Markers placed by multiple users were determined to refer to the same VGLUT1 object if the 3D coordinates of these markers were found within the boundary of the VGLUT1 object.

2.4. Z-axis shrinkage analysis

In order to determine the amount of shrinkage that had occurred to the sample tissue, optical thickness was measured at each time point. The optical thickness of the section was determined by focusing through the tissue section and noting the location where the VGLUT1 signal became stronger than the background signal and then faded

Figure 1

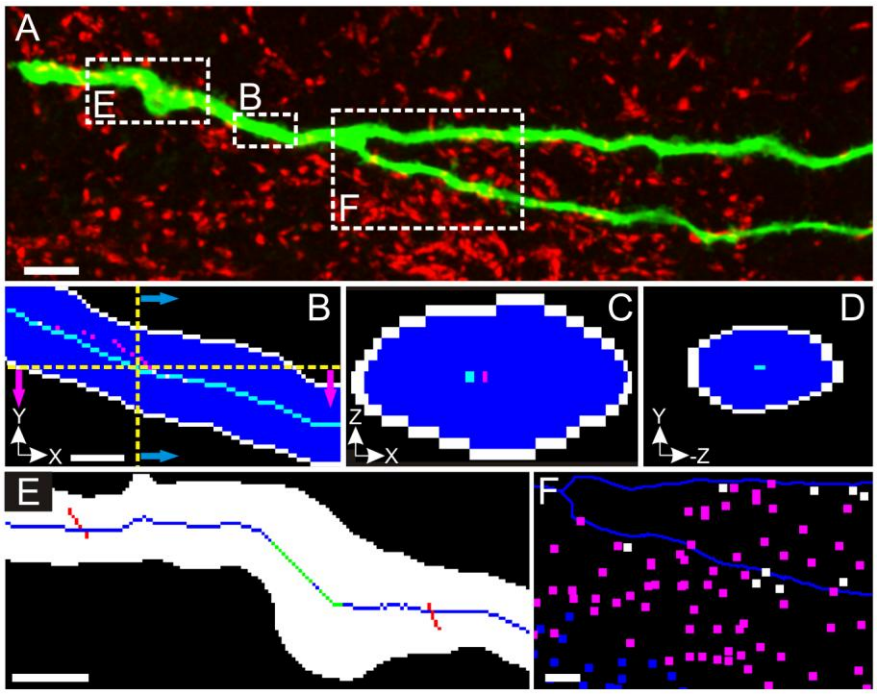

Figure 1. Analysis of confocal image stacks.

A) Maximal intensity projection of confocal image stack showing segment of motor neuron dendrite (green) and VGLUT1 positive synaptic terminals (red). Dashed boxes delineate regions expanded in panels B, E and F. B) XY view of a single optical section from the Z plane. The blue background is the dendrite with white pixels marking the perimeter. Magenta pixels denote the centroids visible in this Z slice from stepping through the Y plane. Cyan pixels denote the centroids visible in this Z slice resulting from stepping through the X plane. White pixels that exist inside of the perimeter are from overlapping centroids determined in the shown X and Y planes. The yellow cross hairs show the location for the slices shown in panels C and D. Magenta and Cyan arrows depict the direction of travel for determining their respective color centroids. C) XZ projection, horizontal line from panel B, of the centroids. D) ZY projection, vertical line from panel B, of the centroids. E) Illustration of centerline determination. Centroid determination along XZ and YZ planes produces some gaps and spurs. Gaps are subsequently bridged along primary axis of dendrite path (green pixels) and a shortest distance, optimal path algorithm eliminates dead-end spurs (red pixels) to determine centerline, illustrated here as a combination of blue and green pixels. F) Enlargement of region surrounding dendrite bifurcation illustrating VGLUT1 objects located inside and outside of the local neighborhood (5.0µm from dendrite). A subset of these objects was found to be synaptic contacts. White pixels indicate locations of VGLUT1 COMs denoted as putative contacts, pink pixels denote VGLUT1 COMs within the 5.0 µm neighborhood, but with distances outside of the acceptable distance. Blue pixels denote locations of the remaining VGLUT1 COMs in the image. Scale bar in A is equal to 5

μm. Scale bar in B applies to panels C and D and is equal to 1 μm. X and Y pixel dimension is 0.08μm while the Z dimension is 0.21μm. Scale bars in E and F equal 2 μm.

back to background levels. The VGLUT1 signal was used since it is expected to be spread throughout the entire tissue section while the backfilled motor neurons can be limited in their location. This percentage was then used as part of the input for the program. The first day of imaging will be used as the control case where the program is run without addressing for z-axis shrinkage. The following three images, day 7, 14 and 28 post cover slip, will be evaluated while addressing for the z-axis shrinkage and without addressing for it. This will allow for comparison of the contacts chosen with and without the z-axis to see if the modification alters the process of contact analysis.

Chapter 3: Implementation of the Semi-Automated Center Distance Algorithm

3.1. Initial image processing

All image processing was performed on a Dell workstation running 64-bit Windows XP (Intel Core2 Quad, Q9450 2.66GHz; 8GB RAM; ATI Radeon HD 4800 series video card with 1GB RAM). Prior to automated synaptic contact analysis, data sets were processed with commands in Imaris XT (version 7.0.0, Bitplane, Zürich, Switzerland) to segment labeled dendrites from background (Figure 2A,B). VGLUT1 signal was also segmented and divided into discrete objects representing individual sensory afferent terminals (Figure 2C,D). Background signals occasionally gave rise to very small VGLUT1 objects (measuring $<0.3\mu m^3$) that were not considered for contact analysis and were automatically filtered out by Imaris. Segmentation was achieved through generation of threshold-based isosurfaces using the "region growing" option in Imaris. This permitted generation of separate VGLUT1 objects for individual synaptic terminals even when several local signal intensity maxima, indicative of multiple terminals, were in close proximity to each other. For each VGLUT1 object, the 3D coordinates of the center of mass (COM), as well as a volume measurement is calculated by Imaris. This information is utilized later in the contact detection algorithm.

Figure 2

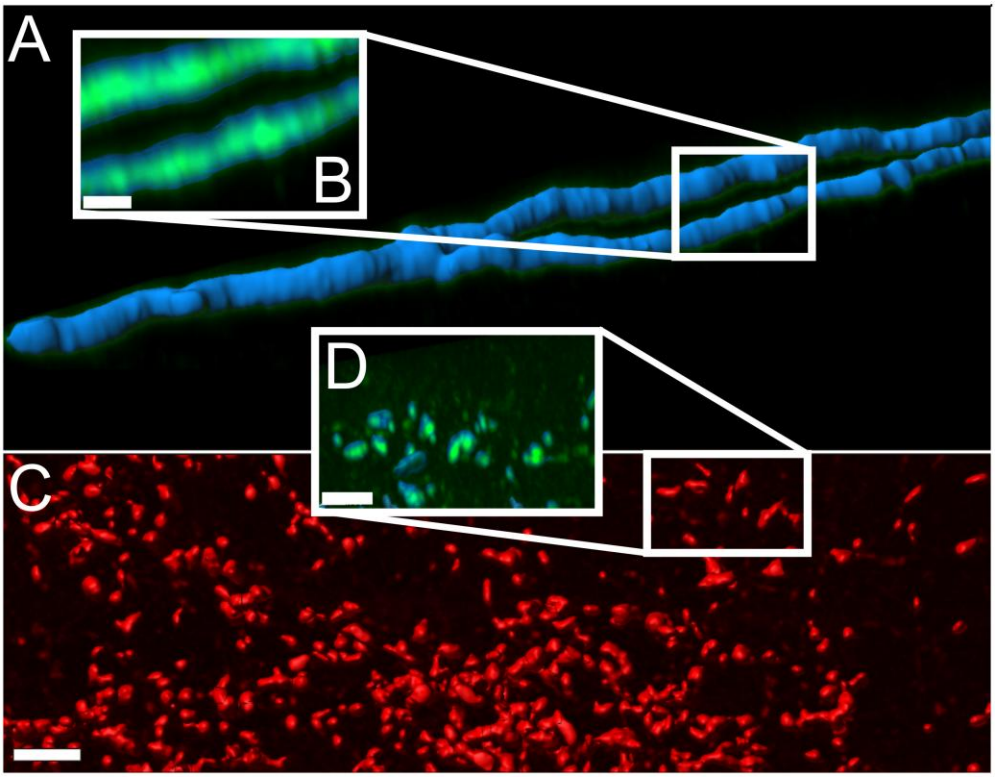

Figure 2: Segmentation of the dendrite and VGLUT1 objects from the image. The motor neuron dendritic segment surface is visible in panel A (blue). Panel B is the insert labeled in panel A and is the result of slightly rotating the image and increasing the transparency of the surface to reveal the fluorescence beneath it. The VGLUT1 segmentation surface is shown in panel C (red). Panel D is the insert labeled in panel C and is the result of slightly rotating the image and increasing the transparency of the surface to reveal the fluorescence beneath it. Scale bar in C applies to A and is 5µm while the scale bar in B is 4µm and the scale bar in D is 2µm.

3.2. Determination of dendrite centerline

It is critical to take into account the 3D nature of the path followed by a dendrite to make valid assessments of distance between a given synaptic contact and the soma of a neuron. A series of algorithms were applied to determine the 3D path of dendrite segments in each image. All algorithms were implemented using custom routines in Matlab (R2009a, Mathworks, Natick, MA).

As described in 3.1, the channel that contains the dendrites of the labeled neuron is segmented and simplified to a binary representation of the dendrite. All voxels determined to belong to the dendrite are set to a value of 1, while all other voxels in the image are set to a value of 0. Using this binary image data, voxels located along the perimeter of the dendrite are identified (for pseudocode of implementation in Matlab see Appendix A, lines 1-5). A perimeter voxel is defined as any voxel with a value of 1 that is connected to at least one voxel with a value of 0. All calculations consider 26-way connectivity for each voxel. Perimeter voxels are stored in a separate binary matrix (*P*), where all non-perimeter voxels are set to zero, but perimeter voxels are set to a value of 1.

A series of centroids of regions bounded by the perimeter voxels are calculated for the three orthogonal planes of the image (XZ, YZ, and XY) (Appendix A, lines 7-18). For example, for each position along the X axis of the image set, the Y and Z coordinates that represent the mean location, or centroid, of all perimeter voxels is calculated (Figure 1B-D). This is illustrated in Equation 1, where $\overline{X}$ is a 3D matrix the size of the original image. For a given X position (i), the average Y and Z coordinates are determined by summing all coordinate values in *P* (denoted by the colon (:) operator) for perimeter

voxels for both the Y and Z dimensions and then dividing by the number of perimeter voxels in that dimension. Depending on the image dimensions, the number of elements in *P* along the Y and Z dimension may not be equal to the number of X elements (*n*). Therefore these dimensions are analyzed from 1 to their respective maximum size (Ym and Zm). $\bar{Y}$ and $\bar{Z}$ are calculated in a similar fashion. The resulting centroid matrices ($\bar{X}, \bar{Y}$, and $\bar{Z}$) are then combined with Boolean OR logic (Appendix A, line 18).

Equation 1: $$\text{for } i = 1 \text{ to } n,\ \bar{X}\left(i, \frac{\sum_{Y=1}^{Ym} Y,\ if\ P(i,Y,:) = 1}{\sum_{Y=1}^{Ym} P(i,Y,:)}, \frac{\sum_{Z=1}^{Zm} Z,\ if\ P(i,:,Z) = 1}{\sum_{Z=1}^{Zm} P(i,:,Z)}\right) = 1$$

Centroid voxels for the three orthogonal planes are the building blocks of the centerline of the dendrite. To accurately measure dendrite length, cumulative 3D distance from the start location is determined at each point of the path. Thus, an unbroken centerline extending the length of the dendrite must be generated from individual centroid locations. To construct this, individual centroid voxels located near the user-defined start point chosen are defined as seed points to begin combining single voxels into segments of connected voxels using 26-way connectivity rules. Centroids from sequential slicing planes are frequently found to be connected with each other using these rules with some segment lengths exceeding 100 voxels. Nevertheless, assembly of individual voxels into segments is unlikely to yield a continuous chain of centroid voxels representing the entire centerline of a dendritic segment. Gaps and breaks are particularly evident at branch points or turns in the dendrite path (Figure 1E).

Lines 20 to 68 of Appendix A present pseudocode for the strategy employed to bridge gaps between centroid segments and to finally form a continuous centerline representing the path of a labeled dendrite. To minimize the computation time required, segments consisting of only a few connected voxels were excluded from further consideration when generating the centerline. We found that exclusion of segments shorter than half the average length of all connected segments did not alter the overall fit of the dendrite centerline path (Appendix A, lines 29-33). If, for example, the average number of connected voxels among all segments in a given image were 20, then segments containing 10 or fewer connected voxels would not be considered in the centerline determination procedure.

The only input required from the user of this program is to identify the initial location in the image to start the dendrite tracing, as well as to mark the end point of the dendrite (Appendix A, lines 24-28). Multiple end points may be chosen if the dendrite is branched, but only a single start point is allowed. Centroid segments are then numbered and sorted according to proximity to the origin (Appendix A, lines 35-38). Beginning with the segment closest to the user-defined origin of the dendrite, all segments are joined to the growing parent centerline structure (Appendix A, lines 39-45). Gaps between segments are bridged by employing a 3D variation of the Bresenham algorithm (Xiong et al., 2006) to link the end of a particular segment to the start coordinate of the next closest segment (Appendix A, lines 46-68).

After all segments have been connected and any gaps filled in, a continuous structure of voxels connects the dendrite origin to one or more end points. This structure, however, usually contains numerous, short side branches that do not follow the overall

path of the dendrite in 3D space. We used a recursive programming strategy to identify the shortest path from the origin to each stop location (Appendix A, lines 70-100). This strategy utilizes a hierarchy of preferred movement direction cases, based on 26-way connectivity and the overall vector connecting the user-defined start and end locations, to advance from voxel to voxel along the branched centerline (Appendix A, lines 76-85). If an end point voxel is encountered that is not one of the dendrite end locations defined by the user (i.e. a dead end on a side branch), the path is retraced to the previous branch decision point and the next alternative route is tested (Appendix A, lines 86-93). In the end, the sequence of moves that produces the shortest path from the origin to the end of the dendrite is stored and the centerline is complete (Appendix A, lines 96-100).

3.3. Modeling the dendrite

We next utilized the centerline path to generate a representation of the dendrite where the 3D morphology of the dendrite is simplified to a series of connected cylinders of equal length (Appendix A, lines 102-112). The goal of this procedure is to produce a model of the dendrite that can be analyzed in neuronal simulation software programs, such as NEURON and GENESIS, which utilize reduced representations of dendrite surface complexity to ease calculations (Bower and Beeman, 2007; Hines and Carnevale, 1997). To accomplish this, the 3D dendrite path is first divided into units of a defined length (Appendix A, lines 106-112). The size of each cylinder unit or bin can be easily altered in the code of the program (Appendix A, line 105). Smaller bins provide a more accurate representation of dendrite morphology, but also increase processing time for

subsequent computations. We found that a bin length of 5.0μm reasonably balanced these two competing criteria.

The radius of each cylinder is algebraically derived from a measurement of the dendrite's volume between unit length nodes. The volume of each 5.0μm length of dendrite is calculated as the sum of the number of voxels that comprise the dendrite located within one 5.0μm bin. To accomplish this, all voxels in the dendrite are labeled using an adapted version of the voxel-scooping technique (Rodriguez et al., 2009). First, all voxels that make up the dendrite in the binary dendrite matrix are changed from a value of 1 to a value of 0.5 to facilitate identification of unexamined voxels in the following steps (Appendix A, lines 113-116). The voxel that marks the start location for the centerline is then changed to a value of 1 and any neighboring voxels that satisfy 26-way connectivity rules are assigned the value of 2 (Appendix A, lines 118-123). In the next iteration, voxels with a value of 2 are analyzed and any 26-way connected and unexamined voxels, meaning those with a value of 0.5, are assigned the value of 3. This procedure is repeated until all voxels of the dendrite have been assigned an integer value greater than 0 (Appendix A, line 120).

Once all voxels have been assigned a number, the integer values of voxels that correspond to the beginning and end of each 5.0μm segment, as determined by the dendrite centerline path, are used to determine the volume of that segment of dendrite. For example, if voxels corresponding to the beginning and end of a particular bin segment have been assigned integer values of 100 and 150, respectively, all voxels with integers values between 100 and 150 would belong to that 5.0μm bin segment (Appendix A, lines 127-137). The volume of that particular bin ($Volume_{bin}$) would be equal to the

total number of voxels belonging to that segment, multiplied by a factor that corresponds to the volume of a single voxel in the data set (Appendix A, line 138). The radius (*r*) of an equivalent cylinder is calculated as: $r = (Volume_{bin}/\pi h)^{1/2}$), where (*h*) is the unit length of each bin, 5.0µm in this case, or the remaining length of a dendrite segment if it is less than 5µm (Appendix A, lines 139-142).

3.4. Modeling the VGLUT1 objects

At this point, information regarding the synaptic marker of interest (VGLUT1) is considered. Pre-processing of image data described in section 2.4.1 yields a discrete object for each putative synaptic terminal, together with 3D coordinates of the center of mass (COM) of that object and a measurement of volume ($Volume_{contact}$) derived from the object's size (Appendix A, lines 144-146). We have chosen to model synaptic markers as spheres with radii (*r*) calculated from the measured volume as:
($r = (3Volume_{contact}/4\pi)^{1/3}$) (Appendix A, lines 147-151). Approximation of synaptic terminals as spheres provides a significant enhancement in analysis efficiency when hundreds of terminals must be analyzed in a single image.

3.5. Z-axis Shrinkage

Z-axis shrinkage is the physical compression of the tissue along the z-axis. From practical experience this shrinkage occurs over time primarily from the cover slip sitting on top of the tissue on the slide. Distortion introduced by this compression is generally compounded by the relatively low axial resolution of the microscope when imaging. Primarily this will affect users who do not image their tissue promptly after mounting and

cover slipping. To account for the shrinkage it is necessary to know the original tissue thickness when it was initially plated and then measuring the thickness prior to imaging. This gives us a baseline percent shrinkage, denoted by the following equation:

$$(1-(\text{Current\_Thickness}/\text{Initial\_Thickness}))*100$$

This value can then be placed in the command GUI when choosing to evaluate for the z-axis shrinkage. The percentage is then used throughout the program to linearly extrapolate the actual Z position assuming that there is equal shrinkage along the z-axis. Both the potential contact location and the centerline are adjusted using this extrapolation when the option is chosen.

3.6. Contact determination

Information from the dendrite centerline path, together with dendrite and synaptic object radii, can now be combined in a straightforward algorithm to identify putative synaptic contacts. For the COM of each synaptic terminal, the nearest voxel along the continuous path of the dendrite centerline can be calculated using the 3D form of the standard distance formula (Appendix A, lines 153-163). This distance is measured from the synaptic object COM to the closest voxel along the dendrite centerline (Appendix A, lines 159-160).

Finally, to identify putative synaptic contacts from among the synaptic terminals in the image, the distance from each synaptic marker COM to the nearest voxel on the dendritic path is compared to the combined distance of the radius of the dendrite at that location and the measured radius of the synaptic object in question (Appendix A, lines 165-169). Synaptic objects, VGLUT1-positive terminals in this study, are then identified

as a synaptic contact if the distance from the COM to the nearest voxel of the dendrite centerline is less than or equal to the sum of the two radii (Figure 3). Most synaptic objects in an image will not be identified as putative sites of synaptic contact. In order to simplify visualization of the results of the algorithm, only synaptic objects located within a defined distance, or neighborhood, can be displayed in the final visualization of the data (Figure 1F). In this study, the neighborhood limits were set to include all synaptic terminals located within 5.0μm of the centerline of the dendrite (Appendix A, lines 171-172). Defining a local neighborhood of synaptic terminals could be used to compare the actual synaptic contact density with the number of locally available synaptic terminals. A visual illustration of the center distance algorithm can be found in supplementary video 1 (Appendix C).

3.7. Data output

3.7.1. Basic Output

Multiple forms of output from the algorithm in Matlab are accessible to the user (Appendix A, lines 174-176). The first is a simple report of successful completion, contact counts for each segment, and filenames of Excel spreadsheets that contain additional output parameters is displayed in the Matlab command window.

The first of four Excel spreadsheets contains information about the path. This is a voxel by voxel list of the center point of the traced dendrite's path. It will contain multiple worksheets in the event there were multiple endpoints that were selected, as that yields multiple segments of dendrite for analysis. In addition to the point by point information, each location will have a corresponding radius measurement, cumulative

Figure 3

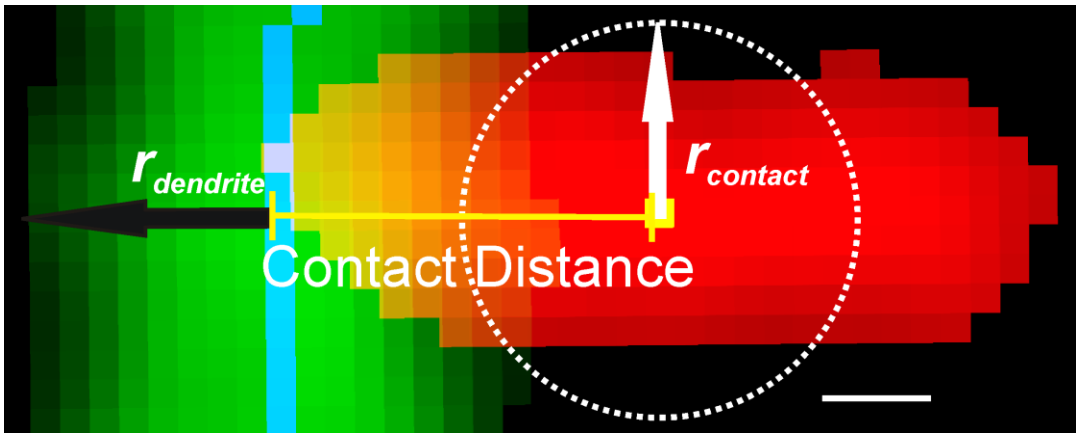

Figure 3. Illustration of center distance method to determine synaptic contacts. Blue line represents the centerline path of the dendrite (green); measured dendrite radius ($r_{dendrite}$) denoted by black arrow. Voxel containing COM of VLGUT1 terminal (red) is shown in yellow. Radius ($r_{contact}$) of dashed circle is determined from 3D surface area of VGLUT1 object. Only a single optical section is shown here. Yellow bar indicates distance between VGLUT1 object COM and nearest point on dendrite centerline. This VLGUT1 terminal was determined to be a synaptic contact, based on the criteria that contact distance is less than the sum of $r_{dendrite}$ and $r_{contact}$. Scale bar equals 0.3µm.

yields multiple segments of dendrite for analysis. In addition to the point by point information, each location will have a corresponding radius measurement, cumulative distance from the start location, the bin number it is associated with and the calculated surface area for that location. This file is automatically generated without any user input and there is currently no means to disable its generation.

The next three Excel files are saved with data relating potential contacts to the path of the dendrite and will also have multiple worksheets if there are multiple dendritic segments being analyzed. Data includes the contact ID number, the position along the path it is closest to, the cumulative 3D distance from the start point to the point of contact, the location of the contact's COM, the distance from the centerline, angle from the XY plane at the point of contact, the radius and the acceptable distance to be ruled a contact. This output is specifically designed to allow for additional analysis without the need to re-run the Matlab routines to regenerate the data. These Excel files are sorted into groups based upon the contact information that is stored in them. The first file will contain the information for only the potential contacts that are ruled as a contact by the program. The second file will contain information about the potential contacts that meet the criteria of being a contact or are within the neighborhood distance the user defined at the start of the program. Finally, the third file contains all of the potential contacts and their relevant information as stated above. These files are only generated when the user is evaluating for potential contacts in the image.

3.7.2. Imaris Output

Output can be directed to Imaris to allow full 3D visualization of the results (Figure 1B, F). This includes the centerline of the dendrite and single pixels that mark the COM for each VLGUT1 object in the image. Each COM is color-coded to denote that object as a synaptic contact (white), belonging to the local neighborhood (pink), or as an object beyond the borders of the neighborhood (blue). Once the COMs are labeled in Imaris it becomes another useful tool as Imaris will allow the user to filter the surfaces on the VLGUT1 single using information from other channels in the image. This effectively allows the user to select all of the VGLUT1 surfaces belonging to a specific group and also supports the use of Boolean logic. Use of Boolean logic would allow to the user to effectively choose just the potential contacts that are within the neighborhood but not ruled as a contact. Output to Imaris is an option that can be turned off if the user wishes to just generate the Excel files or to speed up the speed of the program as output to Imaris can significantly increase run time.

3.7.3. Modeling Output

The final form of output from the program is a specific output for modeling with a program called Neuron Studio (Wearne et al., 2005, Cannon et al., 1998). Neuron Studio is a software package designed to allow users to reconstruct neuronal structures from confocal and multi-photon images. It is a free product available on-line (Appendix C). Neuron Studio utilizes a series of cylindrical structures with a user defined diameter to represent the neuronal structure. This program uses a file extension .swc and has a particular file format; a sample file is shown in appendix B. After the header of the file

Figure 4

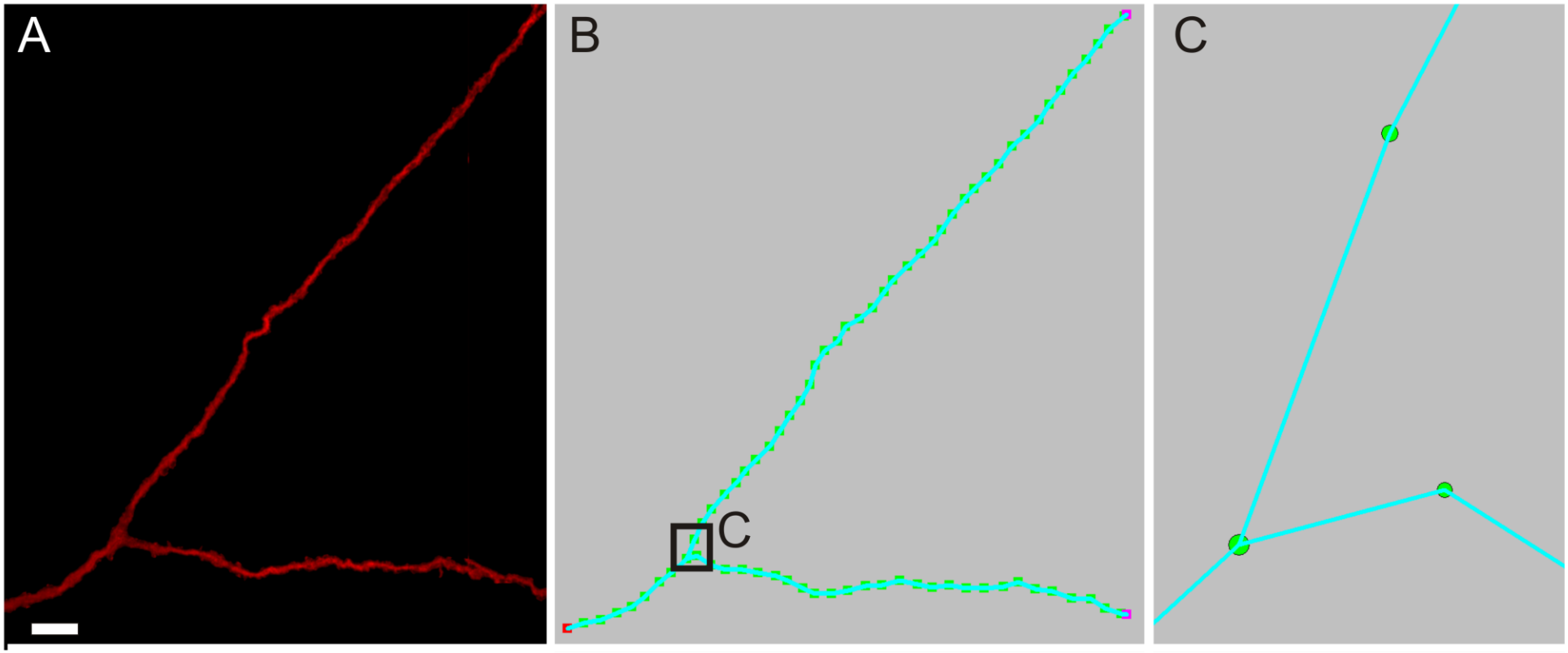

Figure 4. Neuron Studio modeled dendrite compared to the confocal image. Panel A shows the maximum intensity projection of the imaged neuron at day 0. Panel B shows the modeled dendrite data in Neuron Studio in the same orientation as the dendrite in Panel A. Red marks the origin of the dendritic segment while purple marks the end points of each segment. Panel C shows a zoomed in view of the modeled dendrite labeled C in panel B. The zoomed in view shows the individual 5µm segments and the representative markers used by Neuron Studio, note the different sized green circles representing the different radii measurements.

each line is filled in with information that is used to generate the model shown in Figure 4 as it is overlaid on the actual confocal image.

Chapter 4: The Graphical User Interface

Originally the program was designed to operate from the command line in Matlab, which is analogous to running a software program using only DOS. Upon further consideration, a graphical user interface (GUI) was added to this program to increase the ease of user interaction. The GUI is designed to be simplistic in nature and provide a venue for user input and control over the features the program has to offer. Figure 5 is the main window that is used to set all of the parameters necessary for the program to run. Each field must be filled with the appropriate information in order for the program to run. In the event that the user has entered inappropriate or insufficient information they will be prompted to rectify the error when they try to run the program. For instance, the bin size would not make sense if a negative value was entered.

4.1. Designating the File for Analysis

Arrow A in Figure 5 points to the current directory. The current directory will always default to the directory in which Matlab is currently pointing to. This is not likely to be the location where the images are stored for analysis. By clicking on the change directory button (Figure 5, B) the user will be prompted with another window that will allow them to navigate to the location where the

Figure 5

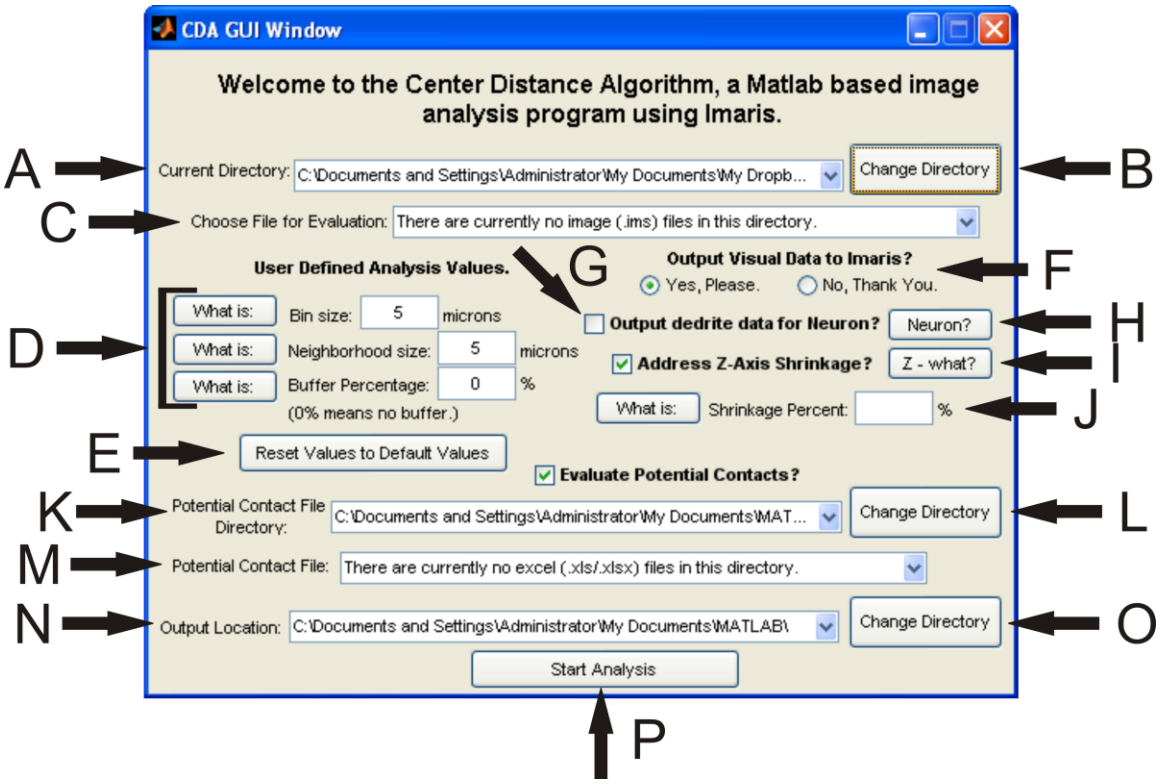
CDA GUI Window
Welcome to the Center Distance Algorithm, a Matlab based image analysis program using Imaris.
A
Current Directory:
C:\Documents and Settings\Administrator\My Documents\My Dropb...
Change Directory
B
C
Choose File for Evaluation:
There are currently no image (.ims) files in this directory.
User Defined Analysis Values.
G
Output Visual Data to Imaris?
F
Yes, Please.
No, Thank You.
D
What is:
Bin size:
5
microns
Output dedrite data for Neuron?
Neuron?
H
What is:
Neighborhood size:
5
microns
Address Z-Axis Shrinkage?
Z - what?
I
What is:
Buffer Percentage:
0
%
(0% means no buffer.)
What is:
Shrinkage Percent:
%
J
E
Reset Values to Default Values
Evaluate Potential Contacts?
K
Potential Contact File Directory:
C:\Documents and Settings\Administrator\My Documents\MAT...
Change Directory
L
M
Potential Contact File:
There are currently no excel (.xls/.xlsx) files in this directory.
N
Output Location:
C:\Documents and Settings\Administrator\My Documents\MATLAB\
Change Directory
O
Start Analysis
P

Figure 5: Main window for the graphical user interface for the Center Distance Algorithm.

This window provides access to all of the variables and options necessary to run the program. The arrows in the image point to the various objects that are interactive within this GUI window.

files are saved. This will then update the value in the current directory line as well as the list containing the available files for evaluation (Figure 5, C). The drop down menu by arrow C will filter all of the files in the current directory and only display those matching valid Imaris extensions. From this list the user is able to choose the file to be analyzed.

4.2. User Defined Analysis Values

Arrow D in Figure 5 is pointing to the area where the user is able to define several integral values used in the program. The "What is:" buttons are essentially on-screen help buttons. When they are pressed a popup window appears and displays information pertinent to the button pressed. This information gives more detail about the variable, what it does and what an acceptable range is for the value. For example, if the user was to push the button next to the bin size box the following message would be displayed;

> "Bin Size is the length that you wish to use when evaluating the different measurements of the dendrite. A small bin will yield more accurate information at the cost of more processing time. The bin size cannot be a negative value."

Likewise the neighborhood size cannot be a negative value either. In the event a negative number is input into either location a popup warning will be displayed bringing this to the user's attention and resetting the value back to the default value. Only the buffer percentage field can have a negative value. In all fields, fractional values expressed in decimal notation will be accepted. In the event the

user wishes to simply reset all of these values back to their default the button marked by arrow E in Figure 5 can be pressed. If the user wishes to change the default values it would be necessary to go into the m-file for the GUI and edit it within designated section of the code.

4.3. Optional Features and Output Control

As discussed in Chapter 2 there are multiple forms of output as well as the option to address the potential tissue shrinkage in the z-axis. Visual output into Imaris can be controlled by selecting the appropriate choice at arrow F in Figure 5 while the option to output the data in a .swc file can be chosen by checking, or unchecking, the corresponding box marked by arrow G. Tissue shrinkage can be considered by marking the "Address Z-Axis Shrinkage" check box. When this box is checked the option to input the shrinkage percent becomes available, marked by arrow J in Figure 5. The last major option is the choice to evaluate for potential contacts. This box is checked by default, but the user can choose not to evaluate for the potential contacts and just get the information about the dendrite. When the box is unchecked the items marked by arrows K, L and M in the Figure will go away. Arrow K is pointing towards the current directory that the excel file with the potential contact information can be found in while M is the drop down menu to choose the file in that location. Arrow L points to the button the user would need to press in order to change the directory and navigate to the one where the file of interest is located. Arrow N points to the area where the path information for the program output is displayed. If the user wishes to change this

output path they would simply click the button marked by arrow O and navigate to the appropriate area. It is possible to create a new folder if the user would desire to do so. Finally once everything is set the user can click the button marked by arrow P to start the analysis. Upon completion of the program this window still remains active with the current settings so the user can easily change files and run the next round quickly without having to change any settings.

4.4. Miscellaneous Windows

During the course of a program run there are several other GUI windows that the user will be able to see and interact with. First, is a dropdown menu to select the channel in the image for analysis (Figure 6). This menu contains a list of all of the available channels in the image with the name that is assigned to them in the Imaris file.

The next is a “yes or no” prompt (Figure 7) for the only remaining element of user input needed to run the program; the selection of the start and stop points. This simple message window asks the user if the point(s) chosen are acceptable. If “no” is chosen, the program loops back to allow the user to reselect the point(s) and then prompts again. If the points are acceptable, the user clicks “yes” and the program will continue.

A progress window (Figure 8) will update periodically to track the various stages of the program run. Three different messages can be displayed next to each of the text labels in this window: '...in progress,' '...completed,' and '...skipped.' The “skipped” status will only appear in the event that the user has

Figure 6


Channel Selection.
Available Channels for Analysis:
Continue

Figure 6: Channel selection window for analysis.

This window is used to select the appropriate channel for analysis in the program. It contains a drop down menu with all of the available channels and the user must select just one from that list to continue.

Figure 7

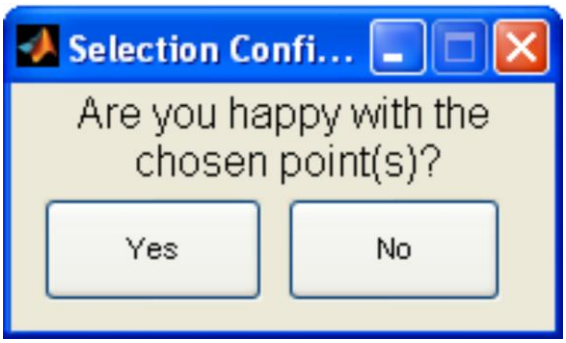

Figure 7: Point selection confirmation window.

This window appears after the user has selected their point(s) in the image. This allows the chance for the user to change their selection without having to restart the program.

Figure 8

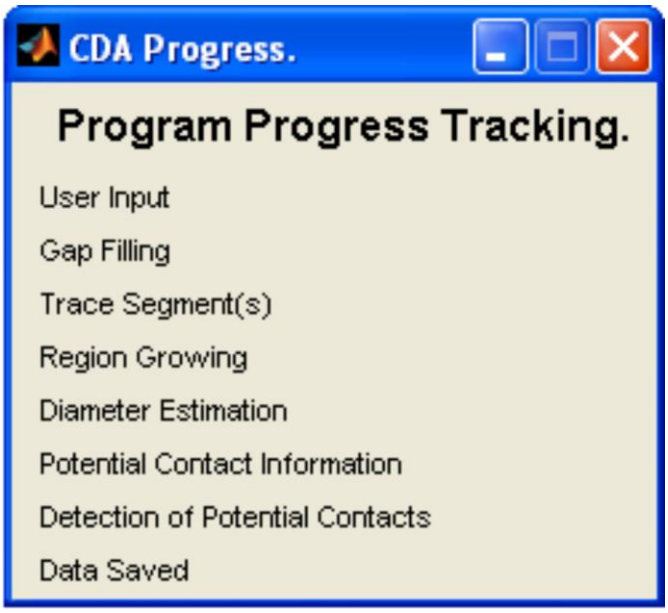
CDA Progress.
Program Progress Tracking.
User Input
Gap Filling
Trace Segment(s)
Region Growing
Diameter Estimation
Potential Contact Information
Detection of Potential Contacts
Data Saved

Figure 8: Program progress tracking window.

This window will display the current status of the program as well as label the completed sections of the program. It provides the user with a means to see that the program is progressing.

chosen not to evaluate potential contacts in the image. This window will automatically close five seconds after the completion of the program and the final data is saved.

The remaining window is an overwrite protection GUI. This will only be triggered if the user is going to potentially overwrite a file that already exists at the target destination. The initial display window is shown in the top panel in Figure 9. The complete path and filename for the file that is potentially being saved is displayed (Figure 9, arrow A). The user may click the dropdown box to see the full name if it is truncated in the display. The user now has three potential options. First, the user can opt to not save the file at all (Figure 9, arrow B). In this case the file will be discarded and the information lost. Second, the user can force the program to simply overwrite the existing file (Figure 9, arrow C). This option will essentially delete the existing file and save the current information in its place. Lastly, the user may choose to rename the file (Figure 9, arrow D). If the user chooses this, the window will change and display the objects marked by arrows E, F, G, H and K. Now the user chooses to change the path, arrow F, in which case they will be presented with another window where they can navigate to the new destination. At this point the user may save the file by clicking on the done button (Figure 9, arrow K). However, the user may wish to change the filename. Selecting the edit name button (Figure 9, arrow H) displays an edit box where the user can rename the file (Figure 9, arrow I). The new name cannot be the same as the original, and if the user attempts to use the same name a warning message will be displayed. Arrow J just serves as a reminder of what file

Figure 9

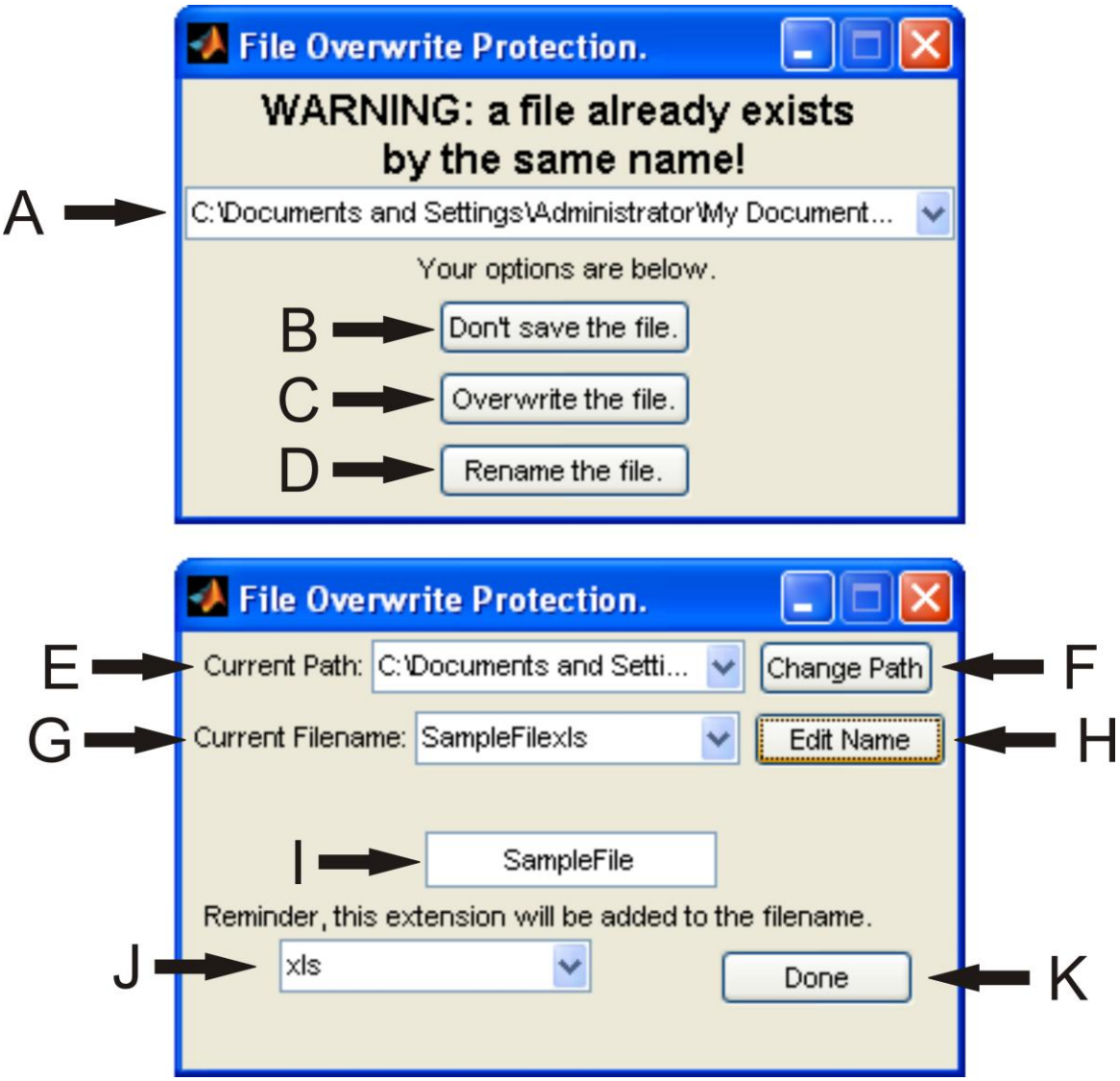
File Overwrite Protection.
WARNING: a file already exists by the same name!
A
C:\Documents and Settings\Administrator\My Document...
Your options are below.
B
Don't save the file.
C
Overwrite the file.
D
Rename the file.
File Overwrite Protection.
E
Current Path:
C:\Documents and Setti...
Change Path
F
G
Current Filename:
SampleFilexls
Edit Name
H
I
SampleFile
Reminder, this extension will be added to the filename.
J
xls
Done
K

Figure 9: File overwrite protection window

This window is only prompted in the event that the user is going to overwrite an existing file. It then allows multiple options for the user to proceed.

extension is going to be appended to the filename and cannot be edited. When the rename is complete, the user can click done, arrow K, and complete the save process. It is important to note that the user has the option to change the location only, change only the filename, or opt to change both the save location and filename with this process.

Chapter 5: Results

5.1. Center Distance Algorithm

To test the performance of our contact detection algorithm, we determined the synaptic contact density of primary sensory afferent terminals on dendrites of individually labeled motor neurons in 3D confocal data sets. Primary sensory afferent synaptic contacts were identified by the presence of VGLUT1, a vesicular glutamate transporter isoform enriched in synaptic terminals of primary sensory afferents (Alvarez et al., 2004; Todd et al., 2003). We compared the number of synaptic contacts detected by the center distance algorithm with the number detected by manual inspection of 10 confocal image data sets using Neurolucida.

First, the 10 test data sets were manually analyzed using Neurolucida by four independent users. Analyzing individual optical sections, users applied criteria described in Chapter 2 to reconstruct locations of VGLUT1 contacts on dendrite segments. Across the 10 images, the total number of contacts identified by the four users averaged 116.25 ± 3.5 (Figure 11A; n = 4 users; all average data is reported as mean ± standard error of the mean). Two users also traced the dendrite in 3D to estimate the path length of the dendrite, and the total length of all segments was estimated to be 805.55 (n = 2 users). In general, there was agreement among users as to whether a particular VGLUT1 object represented a synaptic contact, but not all synaptic contacts were identified by all users. To

compare the results of manual identification with our center distance algorithm, we focused on the subset of VGLUT1 objects that were identified as a synaptic contact by at least 3 of the 4 users (hereafter referred to as majority user contacts; Figure 10A). This data set consisted of 93 contacts across the ten test images (Figure 11A).

The center distance algorithm identified a total of 101 synaptic contacts across the same 10 test images (Figure 11A). Most synaptic contacts were identified by both manual and algorithm strategies; however, a number of contacts were identified by only one approach (Figure 10A, B). The total 3D path length of the dendrite segments across the ten data sets was also measured by the algorithm. This distance (1016.53μm) was approximately 25% greater than the value estimated by users in Neurolucida. Manual dendrite tracing calculates the 3D path length of a dendrite as the sum of distances between limited numbers of nodes placed by the user. Our algorithm also calculates the distance between nodes, but the nodes are the centers of adjacent voxels along the centerline path. The greater number of nodes used in the algorithm likely accounts for the difference in measured 3D path length.

Contacts identified through manual analysis, but not detected by the algorithm, are of particular interest in testing the validity of our algorithm (Figure 5A, B). We re-evaluated these contacts by manual inspection of the image stacks. Instead of relying only on analysis of optical sections along the XY plane, we checked for VGLUT1 terminal apposition to the dendrite along the XZ and YZ planes. In many cases, these orthogonal planes revealed gaps between the

Figure 10

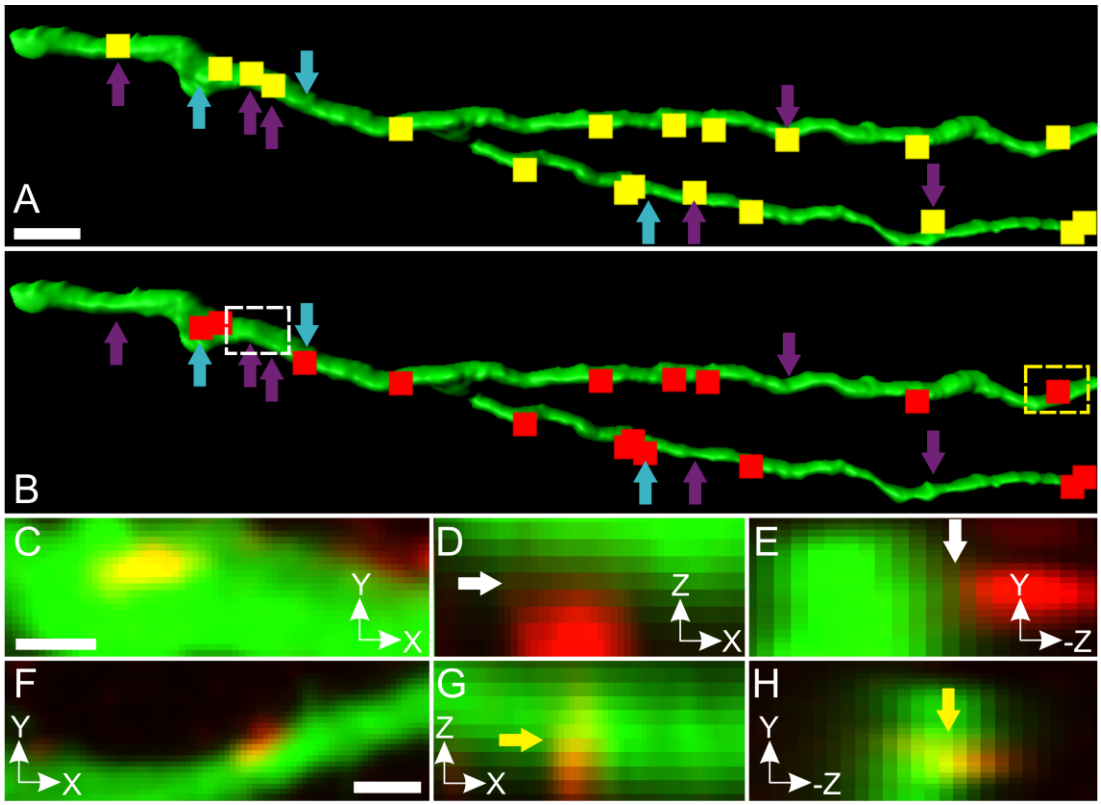

Figure 10. Comparison of manual inspection and center distance methods of synaptic contact identification.

A) Isosurface representation of dendrite (green) with locations of synaptic contacts identified by the majority (at least 3 out of 4) independent users shown with yellow boxes. Purple arrows indicate synaptic contacts identified by manual inspection, but not detected by center distance algorithm. Turquoise arrows indicate synaptic contacts identified by center distance method, but not manual inspection. B) Results of the center distance algorithm method of synaptic contact detection. Contact locations are indicated by red boxes. Dashed white box indicates region highlighted in C-E. Dashed yellow box indicates region highlighted in F-H. C) Raw deconvolved confocal data of single optical section in XY plane where overlap of green (dendrite) and red (VGLUT1) signals would suggest this to be a synaptic contact by our criteria for manual identification (see panel A). (D, E) Alternative views of same region from different planes ([D] XZ, [E] YZ). Gaps between VGLUT1 and dendrite signals are visible (white arrows) and suggest this terminal does not make synaptic contact as indicated in (A). Center distance algorithm did not identify this VGLUT1 terminal as a synaptic contact (see panel B). F) Raw deconvolved confocal data of a single optical section in XY plane where overlap of green (dendrite) and red (VGLUT1) signals, again, suggest this is a synaptic contact. (G, H) Alternative views of the same region from different planes ([G] XZ, [H] YZ). Yellow indicates colocalization of the green and red signals (yellow arrows) indicating this is a contact. The scale

bar in A applies also to B and is equal to 5µm. Scale bar in C applies to D and E and is equal to 1µm. Scale bar in F applies to G and H and is equal to 1µm.

VGLUT1 object and the dendrite which were not observable when viewed only from the XY plane (Figure 10C-E).

We next sought to quantify potential differences between VGLUT1 contacts identified manually and those identified with the center distance algorithm. One criterion for manual identification of synaptic contacts was the presence of yellow pixels in at least one XY optical section, which signified overlap between the fluorescent signals emitted from the dendrite (green) and VGLUT1 terminal (red). As illustrated by the example in Figure 10C-E, overlap in the only the XY plane does not necessarily indicate synaptic contact. Nevertheless, synaptic contacts will likely include regions in the image where a voxel, or group of voxels, contain signal from both the dendrite and VGLUT1 terminal, although this overlap may be in apparent only in 3D. VGLUT1 objects that intersected the signal of the dendrite would likely be located very close to the dendrite and may be possible synaptic connections (see supplementary video 2, Appendix C). Using this approach, we analyzed the 8 test data sets again and defined VGLUT1 objects that shared at least one voxel with the dendrite as putative synaptic contacts. Using only this criterion, a total of 152 putative synaptic contacts were identified in the 10 test data sets (Figure 11A).

Determining synaptic contacts as VGLUT1 objects that intersected the dendrite has the advantage of being free from user bias, but this criterion alone may be less discriminating than manual analysis, as evidenced by the larger numbers of putative contacts detected. In order to characterize this more

Figure 11

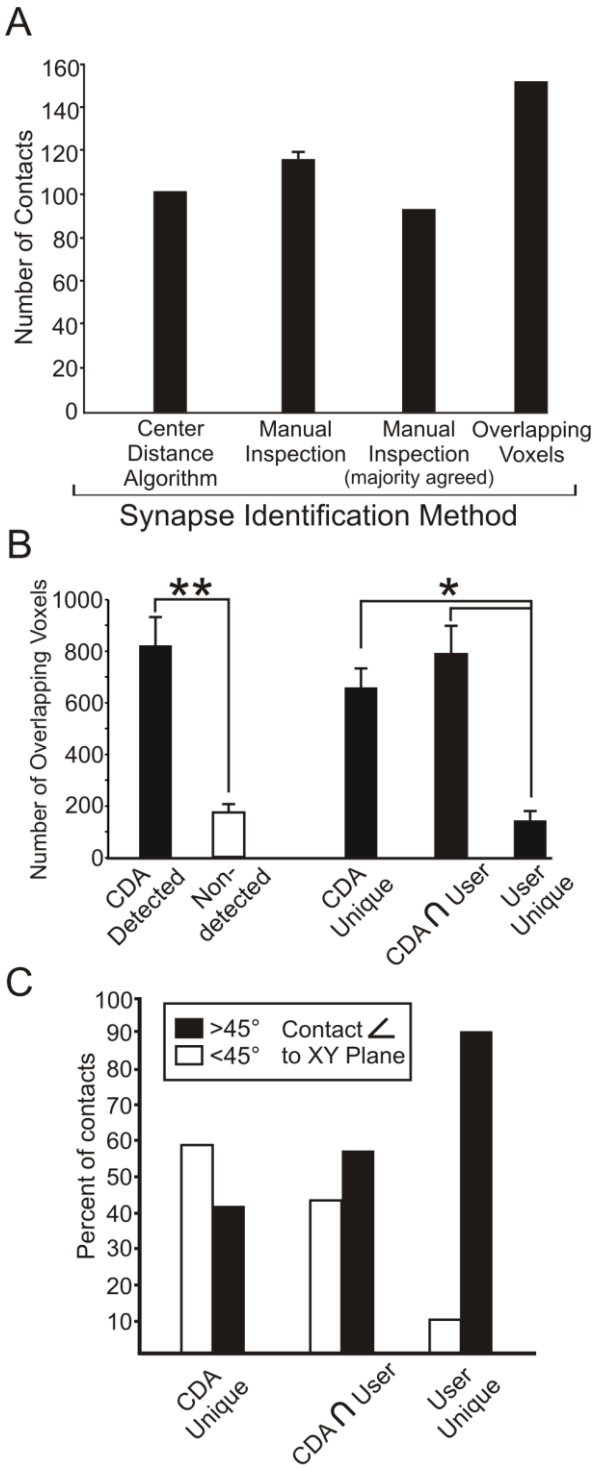
A
Number of Contacts
160
140
120
100
80
60
40
20
0
Center Distance Algorithm
Manual Inspection
Manual Inspection (majority agreed)
Overlapping Voxels
Synapse Identification Method
B
Number of Overlapping Voxels
1000
800
600
400
200
0
**
*
CDA Detected
Non-detected
CDA Unique
CDA ∩ User
User Unique
C
Percent of contacts
100
90
80
70
60
50
40
30
20
10
>45° Contact ∠
<45° to XY Plane
CDA Unique
CDA ∩ User
User Unique

Figure 11. Quantitative evaluation of center distance method of synaptic contact identification.

A) Total number of VGLUT1 synaptic contacts detected in 10 images by different synapse identification methods: the center distance algorithm (CDA), manual inspection and by intersection of overlapping voxels. Data for manual inspection method shows average number of contacts detected by four users ± SEM. The number of majority agreed contacts is the number of contacts identified by at least 3 of the 4 independent users. B) Evaluation of overlapping voxel technique for synaptic contact detection. Average number of overlapping voxels for contacts identified by both center distance algorithm and overlapping voxel technique (black bar; mean ± SEM) is significantly greater than number of overlapping voxels of contacts detected by this strategy, but not detected by center distance algorithm (white bar). Average number of overlapping voxels for contacts chosen only by the CDA (CDA Unique), majority user contacts (User Unique), and those chosen by both strategies (CDA ∩ User) are also shown (mean ± SEM). Double asterisk (**) indicates $p < 0.001$, single asterisk (*) indicates $p < 0.05$. C) The angle relative to the XY plane was measured for each detected contact in the 10 test images. The percentage of contacts with angles greater than 45° (black bar) or less than 45° (white bar) are shown for each detection category (CDA Unique, CDA ∩ User, User Unique).

extensively, we compared the numbers of overlapping voxels, or the extent of overlap, for all VGLUT1 objects defined as contacts by the voxel overlap criterion, with the degree of overlap for synaptic contacts identified by our center distance algorithm. The total number of synaptic contacts identified by the center distance algorithm across the 10 test data sets was 101, or approximately 66% of the number of contacts determined by voxel overlap. All 101 contacts detected by the algorithm fulfilled the criterion of having at least one voxel shared between the dendrite and VGLUT1 object. This is in contrast to the set of manually identified contacts. In this case, 7 of the 93 VGLUT1 contacts identified by the majority of users did not share even a single voxel with the dendrite. For the portion of voxel overlap detected contacts that were also detected by the center distance algorithm (101 out of 152), the average number of overlapping voxels was 816.3 ± 111.3 (Figure 11B). Based on the voxel dimensions of our data set, this corresponds to an average overlap of 1.097 μm^3. This is in contrast to the significantly smaller amount of voxel overlap (167.6 ± 30.2 voxels, for an average of 0.225 μm^3; $p < 0.001$, t-test) observed for the remaining portion of the voxel overlap detected contacts (51 out of 152).

While approximately the same number of contacts was detected by the majority of manual users (93) as by the center distance algorithm (101), we asked what percent of contacts from one data analysis strategy was also detected by the other strategy. We compared the individual VGLUT1 objects identified by manual inspection and found that ~75% of the 93 manually identified contacts were also identified by the center distance algorithm, while the remaining 25%

were detected only in the manual analysis (Table 1). Of the 101 contacts detected by the center distance algorithm, ~30% were uniquely identified by the algorithm. Analysis of the number of voxels overlapping with the dendrite showed that contacts identified by both strategies had an amount of voxel overlap similar to that of the total population of contacts detected by the center distance algorithm (784.9 ± 106.8 voxels, n = 72; Figure 11B). Contacts uniquely detected by the center distance algorithm also had a high degree of overlap (653.8 ± 73.7 voxels, n = 30; Figure 11B). In contrast, the set of contacts uniquely detected by manual inspection had significantly less voxel overlap than the set of contacts uniquely identified by the center distance algorithm, as well as the shared group of contacts detected by both methods (139.1 ± 36.3 voxels, n= 21, $p<0.05$, ANOVA followed by Tukey's tests for multiple comparisons; Figure 11B).

Synaptic contacts may be situated above, below, or to the side of the dendrite in 3D confocal images, and the position of a pre-synaptic terminal relative to the dendrite may influence the probability of being identified as a synaptic contact. We therefore analyzed the spatial distribution of putative contacts identified by different analysis methods. We measured the angle from the XY optical section plane of a line that would connect the COM of each VGLUT1 synaptic contact with the dendrite centerline voxel closest to that VGLUT1 object. The absolute values of contact angles ranged from 0° (contact located in the XY plane) to 90° (contact located directly above or below the centerline in the XY plane). Data shown in Figure 11C is clustered into two groups, the percent of contacts with angles <45° and those with angles >45°. The

set of user majority contacts also detected the center distance algorithm (72 of 93 contacts) were approximately split between these two groups (~43% <45°; ~57% >45°). Contacts detected only by the center distance algorithm were also present in both groups (29 contacts, ~59% <45°; ~41% >45°). The set of majority user contacts not also identified by the center distance algorithm showed a skewed distribution. Only 2 of 21 (~9.5%) majority user unique contacts had angles less than 45°.

The central requirement of the center distance algorithm is that the distance between the COM of a synaptic marker object and the nearest point on the centerline of the dendrite, must be less than the combined radii of the synaptic object and the dendrite at that location. The absolute magnitude of this distance varies with the size of each VGLUT1 object and is also dependent on the size of the dendrite at the proposed point of contact. If, for example, a given VGLUT1 object had a radius of 0.5µm and the radius of the dendrite at the point along the centerline nearest to that object had a radius of 1.0µm, then the distance between the COM for that VGLUT1 object and the centerline would have to be less than or equal to the acceptable distance of 1.5µm (0.5 + 1.0 = 1.5µm) to be considered as synaptic contact. Across all VGLUT1 objects in our data set, whether or not they were identified as synaptic contacts, the mean acceptable distance under these criteria was 1.060 ± 0.004 µm (n = 2440).

The number of detected contacts should vary with changes in the acceptable distance. Figure 12 shows the results of varying the acceptable distance in successive runs of the algorithm on the fraction of manually identified

contacts also detected by the center distance algorithm. This was accomplished by either increasing or decreasing the acceptable distance by a small percentage calculated as, $(r_{dendrite} + r_{contact}) \pm \frac{X}{100}(r_{dendrite} + r_{contact}), X = \%\, change$. As might be expected, the fraction of user majority contacts also detected by the center distance algorithm increases with reduced stringency of the acceptable distance requirement (i.e. as acceptable distance increases). Not all manually identified contacts are detected, however. Even with a 50% increase in the acceptable distance, approximately 7.5% of user majority contacts (7 of 93) are not detected with the center distance algorithm (see Figure 12 and Table 1). Table 1 also indicates the number of center distance detected contacts that do not contain even a single voxel of overlap with the dendrite with increasing acceptable distance. For this data set, some contacts are detected by the center distance algorithm that do not share voxels with the dendrite beginning at 10% increased acceptable distance. While this subset of contacts is always a minor fraction of contacts detected by the algorithm, the frequency of these events steadily increases with increased acceptable distance.

5.2. Z-Axis Shrinkage

In order to test the performance of our adaptation for the Z-axis shrinkage, a series of images were taken at different time points after the tissue was placed under the cover slip. It is expected that over time the cover slip will begin to compress the tissue, due to gravity and the fact that there is nothing rigid to hold the cover slip above the tissue. This may have an effect on the tissue due to

Table 1

% change acceptable distance	CDA	CDA ∩ Users	CDA w/voxel overlap
−20%	77	56	77
−15%	84	61	84
−10%	87	64	87
−5%	95	69	95
0%	101	72	101
5%	103	72	103
10%	111	75	109
15%	119	77	115
20%	125	80	118
25%	135	81	124
30%	142	81	124
35%	158	84	129
40%	170	84	132
45%	176	84	135
50%	186	86	139

Table 1. Percent change in acceptable distance data.

The numbers of synaptic contacts identified by the center distance algorithm (CDA) varies with the percent change in the acceptable contact distance. The number of CDA detected contacts also detected by the majority of manual inspection users is also presented (CDA ∩ Users). Note that a 10% or larger increase in the acceptable distance results in contacts detected by CDA that lack any overlapping voxels with the dendrite (column 4).

Figure 12

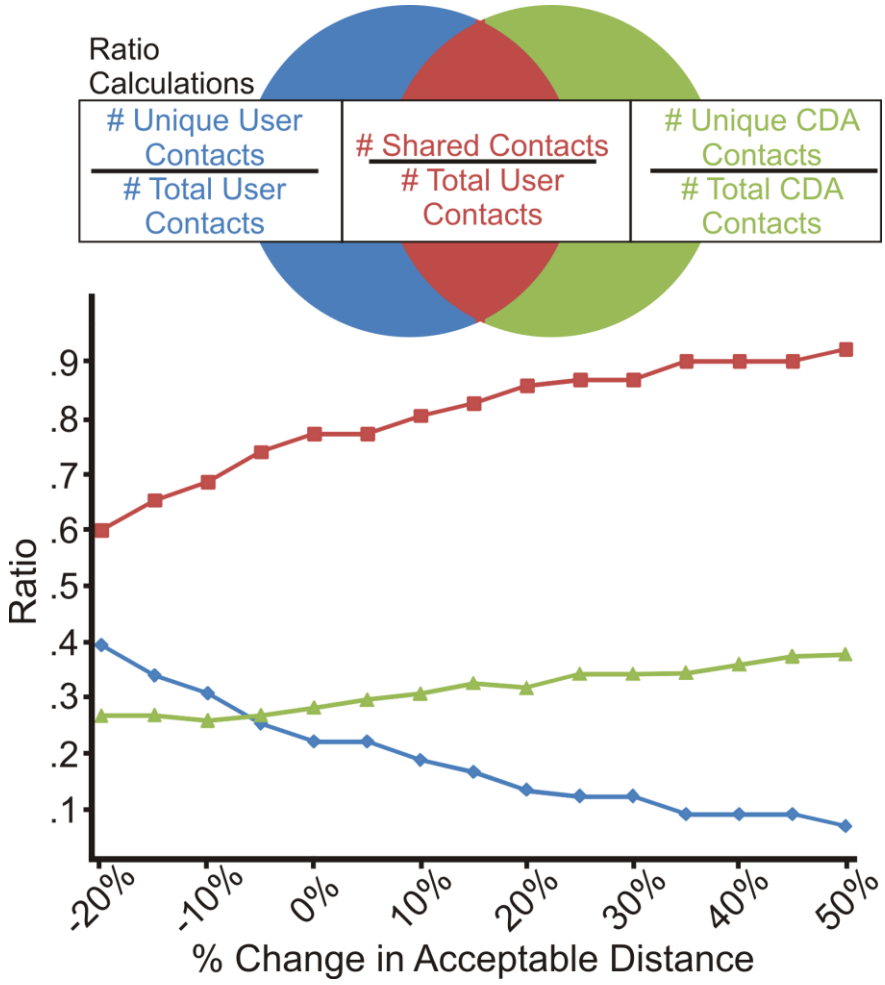
Ratio Calculations
Unique User Contacts / # Total User Contacts
Shared Contacts / # Total User Contacts
Unique CDA Contacts / # Total CDA Contacts
Ratio
.9
.8
.7
.6
.5
.4
.3
.2
.1
-20%
-10%
0%
10%
20%
30%
40%
50%
% Change in Acceptable Distance

Figure 12. Quantitative evaluation of center distance method of synaptic contact identification with respect to changes in acceptable distance.

Venn diagram depicts two separate pools of contacts and their intersection: contacts chosen by the majority of users (User Contacts) and contacts detected by the center distance algorithm (CDA Contacts). Percent changes in the acceptable distance for contact determination were evaluated (negative changes are more stringent criteria and more positive changes are less stringent criteria for contact determination) and changes in the proportion of each side of the Venn diagram were quantified with the respective ratio shown in matching color and position. The number of User Contacts was a constant at 93. The number of CDA detected contacts and the number of these contacts shared with the set of User Contacts varied with the percent change in acceptable distance and can be seen in Table 1. The ratios of these groups are plotted against changes in acceptable distance. The red line related the ratio of shared contacts, relative to the number of User Contacts. The blue line relates the ratio of CDA detected contacts that are not shared with the User Contacts, while the green line depicts the fraction of User Contacts that are not also selected by the CDA.

changes in shape and position of the VGLUT1 potential contacts and the dendrite. Time points of 0, 7, 14 and 28 days post cover slipping were chosen and images taken on each of those days. In our test section, the initial tissue thickness at day 0 was measured to be 32µm. At day 7 it was measured to be 28µm (12.5% shrinkage) it was measured to be 23µm (28.125% shrinkage) on day 14 and finally measured to be 21µm (34.375% shrinkage) on day 28.

To establish baseline measurements, the center distance algorithm was initially applied without the z-axis shrinkage taken into account. Row A in Figure 13 shows the results of analyzing a single branch of dendrite at each of the time points. Results at day 0 were subsequently compared to results on days 7, 14 and 28. Initial results at day 0 showed 24 contacts along the imaged dendrite. Analysis of day 7 data without addressing for the z-axis shrinkage yielded 25 detected contacts. Of these detected contacts 5 of them were new contacts not detected at day 0. Conversely, there were 4 contacts detected at day 0 that were not detected at day 7. Upon use of the z-axis shrinkage adjustment, two of the extra contacts at day 7 were ruled out, leaving a net gain of 2 contacts with 4 missing contacts when compared with day 0. At day 14 there were 3 extra contacts that were detected and 6 that were missed, compared to day 0. The z-axis shrinkage was able to rule out 4 of the contacts but only 2 of them were actually new contacts, so this resulted in a final result of 1 extra contact and 8 missed contacts all together. Finally at day 28 the initial result was 28 detected contacts of which 8 were extra contacts in comparison and there were 4 missed contacts. After applying the z-axis shrinkage adaptation 3 contacts were ruled

Figure 13

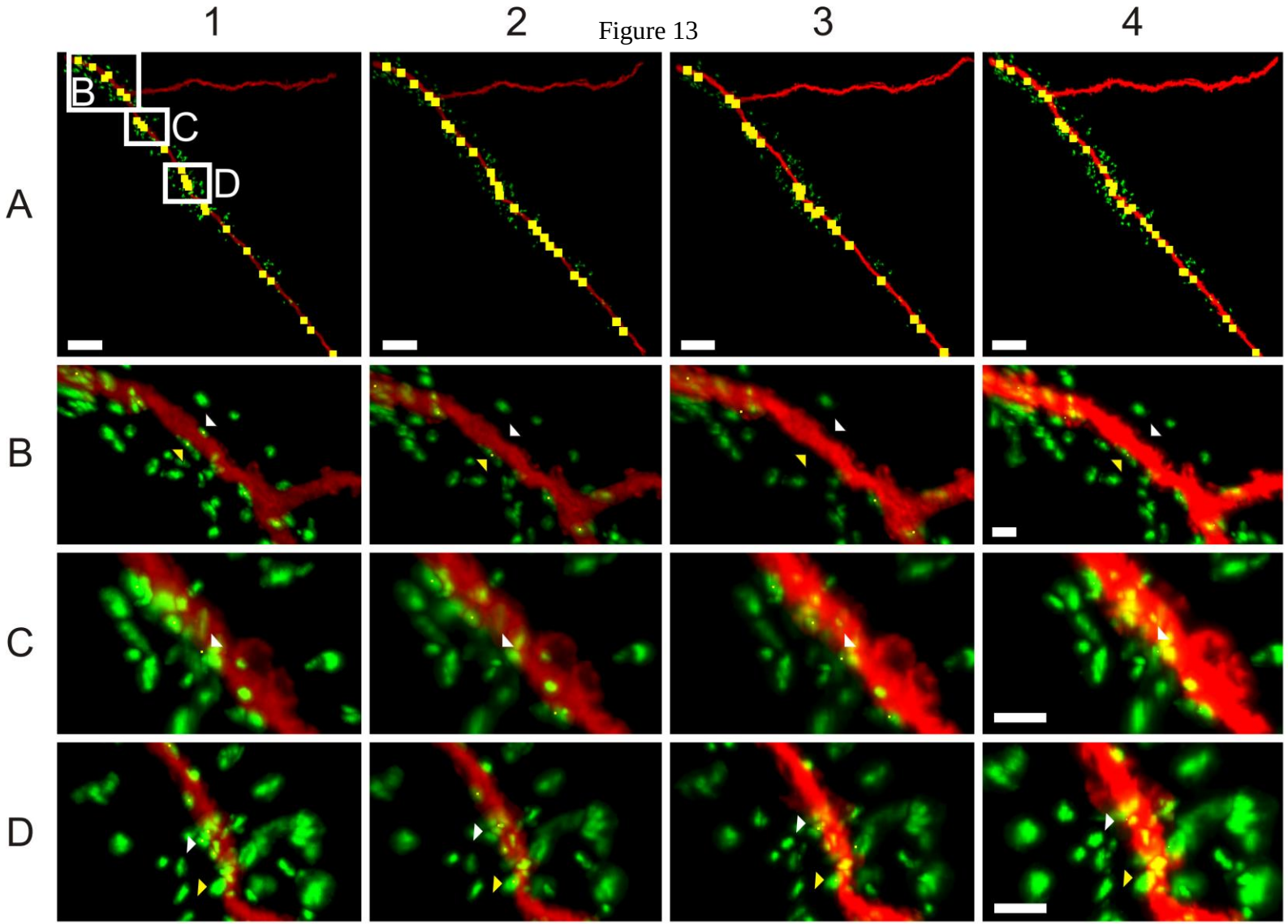

Figure 13: Time course imaging and analysis of potential contacts with the CDA to assess potential Z-axis shrinkage.

The motor neuron dendrite is shown in red, all panels, and is the result of a rhodamine backfill and subsequent immunohistochemistry. The VGLUT1 is shown in green, all panels, and is the result of staining for that protein. Column 1 is the day 0 time point while column 2 is from day 7, column 3 is from day 14 and column 4 is from day 28. Each row relates to the labeled panel it is beneath in row A. Arrowheads in row B indicate approximate location of the labeled contacts from panel B-1 and demonstrate a disappearance of VGLUT1 near the dendrite over a period of time. Row C demonstrates a shift in position of the contact over a period of time. Row D, white arrowhead, notes a shift in location of the VGLUT1 cluster indicated there over time. While the yellow arrowhead marks a potential contact that is determined to be a contact at later time points. In all panels the yellow square indicates the location of the center of mass of a contact as determined by the CDA. Images were taken from the surpass view in Imaris and are not an exact match on a pixel to pixel basis and slight rotation in the image is possible. Scale bars in row A are 15 μm and apply to only their image. The scale bar in B-4 is 3 μm and applies to all of row B while the scale bars in C-4 and D-4 are 1 μm and apply to their respective rows.

out, only one of which was actually an extra contact. Ultimately this shows that the adaptation as it currently stands is unable to fully address the changes to the tissue occurring after the cover slip is put in place and substantial time has passed.

Multiple images of the same area can cause photo-bleaching which would be more prevalent in the FITC channel due to its lower wavelength. This can lead to issues that would arise in the image segmentation stage during the pre-processing. Based upon evidence shown in row B of Figure 13, it is possible that there just isn't a potential contact to be detected in the subsequent days following the initial image. The white arrowhead denotes the location of one contact that is detected in the day 0 image but isn't detected in the subsequent day 7, 14 or 28 image because there isn't any VGLUT1 signal there at all, similarly the yellow arrowhead points to a contact from day 0 that is still present at day 7 but is nowhere to be seen at day 14 and is visible again on day 28's image. However, upon closer analysis of the original data prior to the segmentation in Imaris the missing potential contacts are still present. This means that during the segmentation step Imaris is actually ruling out these potential contacts and not providing the data for the program's analysis. Effects of photo-bleaching, shrinkage or both are likely rendering these VGLUT1 objects too small or too weak to be considered an object by Imaris' algorithm without additional user input during the segmentation step.

Tissue compression over time may also cause slight drifts in the location of individual synaptic terminals. The series of images in Figure 13, row C follow a contact marked by the white arrow head that seems to move just enough to not be detected at day 7 yet is detected at day 14 and 28 but in a slightly different location. This drift of the VGLUT1 potential contacts is further evidenced in row D of Figure 13 by watching the

cluster of contacts labeled by the white arrowhead. This cluster appears to move to the left at day 7 and again at day 14, as noted by the increase in black space between the clusters of VGLUT1 signal. One other potential explanation for this increase in black space is that the VGLUT1 signal is diminished due to bleaching effects since each image is an additional exposure to the laser, despite restricting the laser to <5% of its maximum intensity. However at day 28 the cluster appears to have a different shape than at the prior time points. This suggests that the compression is causing the VGLUT1 objects to drift slightly in the image and is potentially compounded by the effects of photo-bleaching due to the multiple images taken.

Additionally there is evidence of potential contacts being compressed into a location where they are measured as an actual contact following tissue shrinkage (Figure 13, row D). At day 0 the potential contact labeled by the yellow arrowhead is not counted as an actual contact. However in the subsequent day 7, 14 and 28 images this potential contact is ruled as a contact.

Data for each of the detected contacts is listed in Tables 3, 4, 5 and 6 for each respective time point and is the compiled contact information without addressing the z-axis shrinkage. The contact number in each of the Tables can be used to identify the detected contact (Figure 13, row A – yellow markers); starting with contact number 1 in the top left most location along the dendrite and then increasing along the dendrite in down and rightward manner. The + next to the contact number denotes that the contact is in addition to the anticipated contacts from the day 0 image. Additionally, the * next to the contact number denotes contacts that are ruled out by accounting for the z-axis shrinkage.

Additional information including radii measurements, dendrite volume, 3D distance and the number of potential contacts within 5 µm of the dendrite, was also collected during this process and is outlined in Table 6.. There was an observed decrease in dendrite volume for each successive image despite using a standard threshold value for surface determination as suggested by the Imaris software during image preprocessing. The suggested value was used so each image would be minimally subjected to user discretion. Variations in the overall dendrite length from day-to-day is likely due to slight differences in imaging location and the total amount of dendrite being analyzed. It is interesting to note that the average radius of the dendrite appears to be increasing with time and tissue compression. This is most likely due to the fact that any z-axis shrinkage will ultimately distort the normally cylindrical cross section of the dendrites into a more ellipsoidal shape.

Applying the z-axis shrinkage adaptation to the images produced a difference in the measured 3D length of the segment. This difference is only minimal though, as the greatest difference was 4.26% at day 14 after applying the adaptation. The shift in the Z position due to the adaptation is likely responsible for this difference and is to be expected from our linear extrapolation approach.

The discovery that some potential contacts were disappearing in later time point images (Figure 13, row B), led us to investigate properties of individual synaptic terminals in each image. Of particular interest were the parameters of average radius for potential contacts and total number of synaptic terminals detected in the images. It appears that the number of potential contacts falling within the 5µm neighborhood of the dendrite decreases with time until day 28 (Table 6). This could potentially be attributed

Table 2: Day 0 Results								
Contact #	ID	X Pos.	Y Pos.	Z Pos.	Dist. from Path [um]	Angle from XY Plane [deg]	Radius	Acceptable Distance
1	188	41	945	52	1.011511717	-17.25265368	1.18306	1.872323106
2	323	85	925	52	1.291115818	-44.19252069	0.84929	1.474441756
3	411	119	896	45	1.272297099	0	0.933	1.600549784
4	439	131	905	46	0.752396163	-23.49856755	0.72662	1.394172151
5	518	165	856	39	1.406676919	25.24800216	1.19119	1.940842313
6	553	187	836	46	1.500000094	-90	0.94313	1.699222523
7	624	216	767	37	1.170968797	0	0.97847	1.502439668
8	647	229	755	38	1.020881951	-17.0894048	0.89915	1.488047951
9	685	239	744	41	1.789469259	-56.95446084	1.33682	1.869392101
10	840	297	683	18	0.924739974	40.45352829	0.77924	1.303987489
11	999	354	616	21	0.98099546	66.55400238	0.74471	1.211515117
12	1025	364	588	20	0.860743877	44.19252079	0.71436	1.246993716
13	1047	371	568	24	1.307187792	-13.26765539	0.91606	1.473722865
14	1054	374	572	19	1.028383239	61.06393802	1.1859	1.743562173
15	1062	377	561	20	0.914385048	41.00908954	0.76373	1.321398071
16	1216	428	499	13	0.838326921	45.7015219	0.71405	1.251756046
17	1227	433	481	20	1.327478832	-42.68575674	0.87467	1.395383818
18	1410	500	424	18	0.951430553	-71.07501807	0.79554	1.292300448
19	1563	569	350	11	0.430371939	44.19252079	0.69199	1.138612745
20	1665	621	275	13	1.020881951	17.0894048	0.74685	1.241611373
21	1721	649	250	8	0.85877586	20.44661438	0.72344	1.238481897
22	1859	758	120	10	0.922908431	18.96917099	0.83424	1.361414922
23	1897	780	89	10	1.118786819	15.55406893	0.71154	1.178849211
24	2012	856	7	6	1.000220022	64.13206377	0.69563	1.263282421

Table 2: Contact information for the day 0 time point.

This table relates to the large yellow markers shown in row A column 1 of Figure 13. Numbering is oriented to start in the top left of the image and increase along the path of the dendrite. The + next to the contact number denotes that the contact is in addition to the anticipated contacts from the day 0 image. Additionally, the * next to the contact number denotes contacts that are ruled out by accounting for the z-axis shrinkage. The ID number is the number used as reference within Imaris to be able to find the contact quickly. X, Y, and Z position is the center of mass for the contact while distance from the path is a measure of the distance from the center of the dendrite to the center of the contact and must be shorter than the sum of the two radii, the value shown as the acceptable distance. Angle from the XY plane is an indicator of where the contact is in relationship to the center plane of the dendrite. Values can range from 0, directly adjacent, to 90 directly above, and can be negative. Negative values simply mean the object is below the XY plane while positive values are above the plane. There is no indicator from the angle measurement if the contact were to exist in the second or third quadrent. Finally, the radius measurement is the radius of the contact. Radius of the dendrite can be determined by subtracting the radius value from the acceptable distance.

Table 3: Day 7 Results								
Contact #	ID	X Pos.	Y Pos.	Z Pos.	Dist. from Path [um]	Angle from XY Plane [deg]	Radius	Acceptable Distance
1	178	41	951	80	1.18584649	-32.09103593	1.20225	1.81197951
2	323	85	932	79	1.1615076	-32.84706413	0.84217	1.531901044
3	402	122	902	70	1.481914934	8.146723676	1.07529	1.78149606
4	513	166	868	64	1.244012823	19.73176011	1.19566	1.903377873
5	557	188	846	73	1.469999923	-90	0.92841	1.794341769
6	628	218	780	61	1.289511498	-9.372496276	1.02364	1.593997075
7	649	232	767	61	1.062355838	-23.28766338	0.93209	1.493957668
8	684	242	757	65	1.658096429	-49.45604513	1.39458	1.956449677
9+	729	263	730	50	1.550660458	15.71499096	1.0669	1.638901473
10	834	302	700	34	0.908242231	13.36866381	0.80731	1.358635145
11	985	360	633	39	0.741115342	58.2192909	0.80042	1.303312956
12	1022	370	606	37	0.819477853	30.83192874	0.75727	1.331048326
13	1044	381	591	35	1.121550664	48.50062987	1.24728	1.821066159
14	1057	384	579	37	0.807774692	31.32869231	0.82323	1.342286377
15+	1067	388	560	30	1.649618074	39.53213809	1.27578	1.814980243
16	1204	436	519	27	0.819477853	30.83192874	0.75069	1.345805899
17*+	1356	494	466	33	1.43655832	-61.29404687	0.88769	1.443082121
18	1392	509	445	33	0.926256939	-65.07711189	0.85608	1.411471363
19*+	1435	533	423	32	1.094403892	-73.62282238	0.71012	1.245173815
20+	1489	554	394	19	1.219181644	43.549952	0.77049	1.376901516
21	1550	579	373	23	0.605673155	43.90329599	0.73936	1.247818082
22	1638	632	299	27	0.998148256	12.1451834	0.80326	1.323749405
23	1695	661	275	19	0.689999981	0	0.80079	1.350882694
24	1852	772	146	22	0.968586568	25.69761132	0.92795	1.48355343
25	1883	795	115	21	1.017048642	11.91613822	0.80437	1.303086456

Table 3: Contact information for the day 7 time point.

This table relates to the large yellow markers shown in row A column 2 of Figure 13.

For additional details the reader is referred to the legend for Table 2.

Table 4: Day 14 Results								
Contact #	ID	X Pos.	Y Pos.	Z Pos.	Dist. from Path [um]	Angle from XY Plane [deg]	Radius	Acceptable Distance
1	85	22	618	75	1.197514533	-44.54368296	1.40453	2.168958643
2*	142	45	604	75	2.064098114	-45.41219139	1.37035	2.141172382
3	293	107	562	60	1.276524025	9.468726352	1.28332	2.089487814
4*	324	122	550	70	1.692704608	-82.9757452	1.24493	2.000899366
5	369	141	504	57	1.34198254	-9.002925403	1.15755	1.791523395
6	389	150	496	58	1.116974976	-22.08709569	1.08159	1.769468753
7	407	157	487	62	1.902043774	-50.61076897	1.66931	2.357190408
8+	444	171	471	47	1.522781232	16.01035723	1.24482	1.912611961
9	656	249	375	36	0.949256599	12.78103694	1.77512	2.442294323
10	668	255	357	28	1.737206955	57.799215	1.43272	2.091988789
11*+	693	260	370	45	1.838325033	-66.0465159	1.5624	2.221668912
12*	729	275	331	36	1.964337471	-39.89910377	1.21613	1.980956002
13	776	290	317	35	1.572792445	-41.88228392	1.05388	1.787181313
14	802	300	324	38	2.047822259	-55.1232203	1.36933	2.102628798
15*+	870	326	294	31	1.259999975	-90	1.03013	1.684829155
16	894	336	280	31	0.865129455	-76.15650801	0.97017	1.641619057
17	969	366	245	18	1.280442745	29.47325957	0.889	1.526891771
18+	1123	438	166	18	0.360275597	-35.65386273	0.94802	1.638542862
19	1238	512	80	20	1.119768745	34.23691618	1.04536	1.742141421
20	1264	527	59	19	1.116974976	22.08709569	0.93025	1.537476007
21	1370	580	5	17	0.753855427	56.68921363	0.98219	1.949343615

Table 4: Contact information for the day 14 time point.

This table relates to the large yellow markers shown in row A column 3 of Figure 13.

For additional details the reader is referred to the legend for Table 2.

Table 5: Day 28 Results								
Contact #	ID	X Pos.	Y Pos.	Z Pos.	Dist. from Path [um]	Angle from XY Plane [deg]	Radius	Acceptable Distance
1	93	19	628	74	1.342328173	-69.82898851	1.498117229	2.56744308
2*	167	43	613	74	2.21432523	-41.59485847	1.438091683	2.463006037
3	265	74	595	64	1.478698779	8.164563733	1.245900436	2.225761967
4	344	103	571	58	1.390398874	17.58206983	1.322002702	2.390700077
5*	372	119	558	69	1.901301878	-83.74966041	1.327308712	2.44772921
6	425	137	513	56	1.341979521	-9.002945797	1.184082672	2.128722044
7	448	146	504	57	1.116971377	-22.08717053	1.124615248	2.06925462
8	475	152	496	60	1.690949137	-38.38576257	1.743026642	2.684177983
9+	509	167	479	46	1.325446731	0	1.284137913	2.128695175
10	596	193	458	29	1.119767821	34.23694821	1.009866227	1.917330182
11+	717	231	413	34	0.781757635	53.6949737	1.030509509	1.826519167
12	755	243	384	34	0.87893855	13.82307497	2.00872887	2.886186365
13	775	249	364	26	1.682326039	48.50063011	1.512828677	2.370586465
14	796	254	377	43	1.803022423	-68.71223201	1.665905775	2.54336327
15+	838	268	338	34	1.687616726	-29.85081233	1.305123041	2.308505252
16	886	284	324	32	1.399814281	-48.59899656	1.189281537	2.103131215
17*+	917	293	330	36	2.032027773	-68.4512471	1.459922181	2.373771859
18+	996	319	300	28	1.276890333	-80.67046033	1.163404351	2.075125723
19	1020	329	286	28	0.889549307	-70.78641906	1.077972026	1.926005706
20+	1056	345	271	27	1.064936597	-52.07158428	0.902192556	1.685466099
21+	1098	359	251	15	1.215270339	43.72550865	0.92674233	1.816447312
22	1146	375	237	19	0.625015992	42.22028259	0.909562467	1.736291844
23+	1201	404	190	30	1.569206488	-32.36442093	1.098796498	1.958088001
24	1220	409	187	22	1.225139175	9.869756817	1.000573416	1.789883602
25	1269	429	171	14	0.777746768	32.68510366	1.003268677	1.869303477
26	1403	502	83	17	0.951227086	26.20185715	1.095888732	1.992650217
27	1433	517	62	16	1.329687194	28.28096271	1.009007152	1.815742097
28	1538	569	7	14	1.08082469	35.65394247	1.033200129	1.661359338

Table 5: Contact information for the day 28 time point.

This table relates to the large yellow markers shown in row A column 4 of Figure 13.

For additional details the reader is referred to the legend for Table 2.

Table 6

Day 0	
3D length	235.71m
Dendrite Volume	1022.07µm^3
# Potential Contact	174
Avg. Potential Contact Radius	0.91µm
Avg. Dendrite Radius	0.55µm

Day 7		Day 7 w/ Z-axis Shrinkage	
3D length	228.74µm	3D length	234.29µm
Dendrite Volume	924.99µm^3	Dendrite Volume	924.99µm^3
# Potential Contact	167	# Potential Contact	157
Avg. Potential Contact Radius	0.98µm	Avg. Potential Contact Radius	0.98µm
Avg. Dendrite Radius	0.58µm	Avg. Dendrite Radius	0.58µm

Day 14		Day 14 w/ Z-axis Shrinkage	
3D length	222.35µm	3D length	231.84µm
Dendrite Volume	912.06µm^3	Dendrite Volume	912.06µm^3
# Potential Contact	117	# Potential Contact	99
Avg. Potential Contact Radius	1.26µm	Avg. Potential Contact Radius	1.26µm
Avg. Dendrite Radius	0.68µm	Avg. Dendrite Radius	0.68µm

Day 28		Day 28 w/ Z-axis Shrinkage	
3D length	220.22µm	3D length	228.71µm
Dendrite Volume	1850.63µm^3	Dendrite Volume	1850.63µm^3
# Potential Contact	151	# Potential Contact	119
Avg. Potential Contact Radius	1.27µm	Avg. Potential Contact Radius	1.27µm
Avg. Dendrite Radius	0.88µm	Avg. Dendrite Radius	0.88µm

Table 6: Additional measures of image objects.

Day 0, Day 7, Day 14 and Day 28 columns are all values computed without addressing for the z-axis shrinkage. The Day 7 w/ Z-axis Shrinkage, Day 14 w/ Z-axis Shrinkage and Day 28 w/ Z-axis Shrinkage are the value when accounting for the z-axis shrinkage. The 3D length is a measure of the segment that was analyzed in the image. Dendrite volume is the measured volume within the surface in Imaris. The # Potential Contacts is the reported value of potential contacts that are within the neighborhood of the dendrite. In this case that neighborhood is 5 µm. Average potential contact radius is a measure of the overall average in the entire image for the VGLUT1 objects while the average dendrite radius is a measure of just the dendrite that was analyzed.

to variations in image thicknesses from one time point to another. To account for variations in image size, total number of synaptic terminals in each image was normalized to the total image volume. The resulting trend matched the trend showed by the change in potential contacts (those synaptic terminals found within the 5μm radius of the dendrite) in Table 6.

Additionally, the average radius of potential contacts in the day 14 and 28 images was found to be greater than that in either the day 7 or day 0 images (Table 6). Figure 14A shows a histogram of the radius measurements of all of the potential contacts in each of the images at the different time points. Figure 14B shows the cumulative percent as the bin size is increased for the radius measurement. The right shift of the day 14 and 28 data (Figure 14A), is a strong indicator that individual synaptic terminals are potentially close enough in 3D space to be treated as a single synaptic terminal during image preprocessing steps. Combined synaptic terminals would result in fewer potential contacts and have larger volume radius measurements.

Figure 14

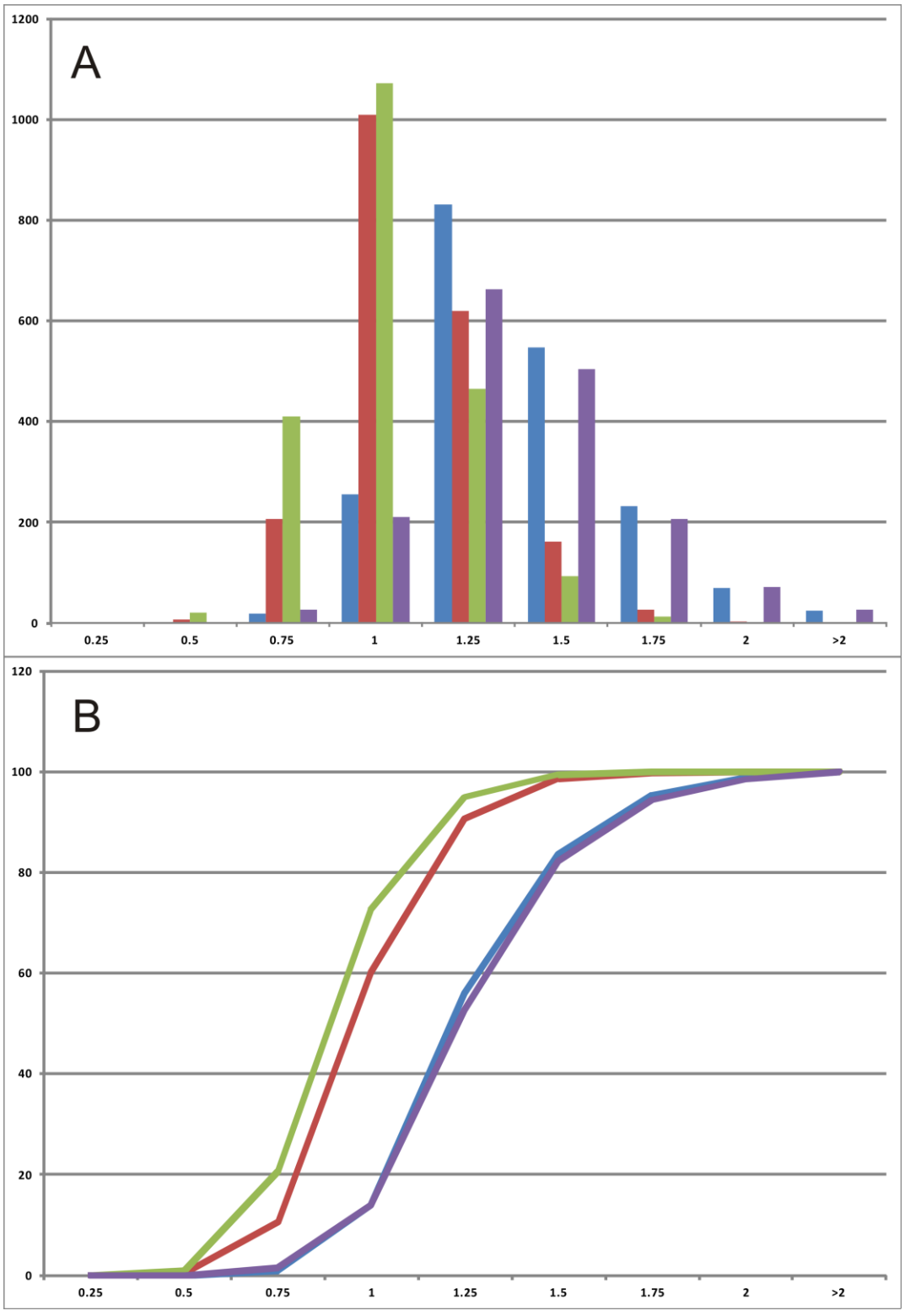
A
1200
1000
800
600
400
200
0
0.25
0.5
0.75
1
1.25
1.5
1.75
2
>2
B
120
100
80
60
40
20
0
0.25
0.5
0.75
1
1.25
1.5
1.75
2
>2

Figure 14: Histogram and cumulative percentage of potential contact radii. Panel A is a histogram of the measured radii of the VGLUT1 potential contacts in each image. The green bars relate to the day 0 image while the red relates to the day 7 the blue relates to the day 14 and the purple relates to the day 28 images. The x-axis is the upper bound of the respective bin size in µm while the y-axis is a simple count of the number of VGLUT1 objects that exist within that bin. Panel B shows the cumulative percentage of total objects as you progress through each subsequent bin. The x-axis is still the bin size, noting the upper bound of the bin in µm while the y-axis is noting the total percentage of objects.

Chapter 6: Discussion

The spatial distribution of synaptic inputs on a particular neuron can have significant effects on the functional output of that cell (Grande et al., 2005; Grande et al., 2010). To date, the process of mapping putative synaptic contacts on neurons has been a time-consuming and primarily manual task. With this project we set out to generate an objective, computer-automated method for rapid identification of synaptic contacts on labeled dendrite of individual neurons from 3D fluorescence imaging data sets. We present an algorithm whereby putative synaptic contacts are determined by comparison of the distance between the centerline of the dendrite and the COM of a given pre-synaptic object. An object is then labeled as a synaptic contact if the distance between these centers is less than a defined acceptable contact distance. This distance is determined to be the radius of the potential synaptic contact plus the radius of the dendrite nearest to that potential contact.

On average, the Matlab code for the algorithm processes 53,000 voxels per second (76.67μm^3/sec) resulting in an average run time of 214 seconds (3.6 minutes) per data set for the ten test data sets in this study. This is in contrast to an average of 615 seconds (10.25 minutes) required to manually analyze the same data sets with Neurolucida. We found the algorithm outperformed manual inspection by even greater margins (up to 6-fold) when analyzing relatively small images. One limitation on the speed of analysis is the number of presynaptic objects present in the image. In a full-

frame image set (1024 x 1024 XY pixel dimensions) there may be hundreds of potential synaptic objects to analyze. While human users can easily ignore synaptic objects located far from the dendrite, the algorithm must first calculate the distance to the nearest point on the dendrite centerline for each potential synaptic contact. When the image is closely cropped during imaged acquisition or pre-processing to fit the shape of the dendrite, the algorithm easily outperforms manual inspection in the time required to analyze each image. However, there is a possible solution to this that has not been explored. This is to utilize the parallel processing toolbox within Matlab which would allow for the use of the processors on the graphics card to speed up calculations (Reese et al., 2011) By using this, the program could easily decrease the time it takes to analyze each potential contact as you would be spreading the millions of calculations across the hundreds of processors on the graphics card instead of just using your single CPU with only a few cores.

In this study, we employed image processing tools available in Imaris, a commercial software package for 3D visualization images, to pre-process images. Intensity-based threshold segmentation of neurobiotin-labeled dendrites and VGLUT1 synaptic terminals was accomplished using isosurface generation together with region-growing functions in Imaris. Measurements of volume and 3D location of the COM for each VGLUT1 object were then readily available and this information was utilized by the algorithm implemented in Matlab. Threshold levels could be altered by the user, but the location of the COM of a VGLUT1 object is relatively insensitive to threshold settings. Implementation of our algorithm is not, however, dependent on image processing strategies of a particular commercial platform. Strategies for isosurface generation have

been described in the literature and could be adapted in Matlab (Rodriguez et al., 2008; Rodriguez et al., 2006; Schmitt et al., 2004). In addition, similar synaptic object segmentation, including region-growing algorithms, could be obtained through custom routines in Matlab (Mehnert and Jackway, 1997). Nevertheless, creating a stand-alone image analysis tool in Matlab was beyond the scope of this project but is something that could be done in the future.

While the center distance algorithm outperforms manual inspection in terms of speed, is it more or less accurate in identifying synaptic contacts? Analysis of several contact parameters identified differences between the two methods that may point to common errors by human users in judging synaptic contacts. Among the population of contacts identified only by manual inspection, the great majority were found to be located at angles greater than 45° from optical plane (XY) that contained the nearest voxel on the dendrite centerline. Synaptic contacts are found above, below, and next to dendrites, but manual judgment of proximity in the XY plane is likely to be less accurate when compounded with the requirement to also judge if two objects are in close proximity in the XZ and/or YZ planes. In contrast, the population of contacts detected only by the algorithm was more evenly distributed in the two bins of contacts with angles greater than or less than 45°. While we cannot definitively conclude that contacts identified only by manual inspection and with angles greater than 45° are more likely to be assigned in error, it does appear that the center distance algorithm is not biased in detecting contacts at various angles from the optical sectioning plane.

We also found that contacts detected only by manual inspection had less voxel overlap with the dendrite than contacts detected by the center distance algorithm. An

overlapping voxel contains signal from both the dendrite and VGLUT1 terminal, suggesting close proximity of the two objects (Wouterlood et al., 2007). Manual inspection was performed in Neurolucida using deconvolved confocal data sets and users were instructed that yellow pixels, derived from combination of VGLUT1 (red) and the dendrite (green), must be observed in order for an object to be defined as a synaptic contact. Image resolution, however, is much greater in the XY plane than in the Z axis. The great majority (~90%) of contacts identified only by manual inspection had significant displacement along the Z-axis from the centerline of the dendrite, as evidence by angles from the optical plane of greater than 45°. Users may have been influenced by apparent overlap of objects in the Z-axis and defined them as synaptic contacts. In contrast, the amount of voxel overlap of the set of contacts detected only by the center distance algorithm was not significantly different from the amount of voxel overlap from the larger set of contacts that were identified by both methods.

The method presented here differs from previous automated methods in that synaptic contacts are determined by distance between pre-synaptic objects and the dendrite. Previous methods have employed two general strategies: intensity mapping and object intersection. Using an intensity mapping approach, the intensity values of a pre-synaptic marker data channel located within a specified distance from the dendrite are projected onto surface representations of dendrites (Evers et al., 2006; Evers et al., 2005; Meseke et al., 2009). Local signal clusters of the pre-synaptic marker are then identified as putative synaptic contacts. An advantage of this method is that calculations regarding possible contacts can be performed directly on the dendrite surface, as the fluorescent signal from the pre-synaptic marker is not treated as a separate object. A disadvantage,

however, is that information regarding potential synaptic contacts is ignored if it falls outside of the analysis zone surrounding the dendrite, which is usually less than 0.4µm (Evers et al., 2006). Correlation of synaptic density or position to physical features of the pre-synaptic terminal, such as volume, is not possible because the physical extent of the terminal likely extends beyond the narrow region around the dendrite surface that is available for analysis. Because the center distance algorithm treats pre-synaptic terminals as separate objects, the volume of an individual contact can be readily calculated. Electron microscopic analysis of sensory afferent terminals on motor neurons indicates significant properties of pre-synaptic terminals are correlated with terminal volume. Amount of terminal surface apposed to the dendrite, number of active zones, and number of vesicles located near the active zones are all positively correlated with terminal volume (Pierce and Mendell, 1993). Admittedly, there are obvious limitations to extrapolation of synaptic efficacy from purely light microscopic morphological analysis; nevertheless such information may enhance computational models of neuronal function derived from reconstructions.

Defining synaptic contacts as regions of intersection between synaptic markers and labeled dendrites are the hallmark of the second general category of automated contact detection strategies. This approach can be rather straightforward in cases where the dendrites of the neuron to be analyzed are relatively planar, such as for retinal ganglion cells. For example, 2D maximal intensity projections of both dendrites and synaptic markers can be combined in a single computational step and clusters of overlapping pixels then are taken to represent locations of synaptic contact (Jeon et al., 2002). This approach is computationally efficient and can be expanded to analysis of 3D

data sets. There is the possibility that "false positives" are detected, but the frequency of these events may depend on the preparation being studied (Wouterlood et al., 2007; Xu et al., 2008). Synaptic objects located close to the dendrite, but not in actual contact, may have some voxel overlap due to the inherent resolution limits of light microscopy, but this can be mitigated by requiring a minimum number of overlapping voxels for an object to be classified as a synaptic contact (Wouterlood et al., 2007). Synaptic contacts identified by the center distance algorithm in our test images had substantial amounts of spatial overlap with the dendrite (averaging ~1.0 μm^3). Therefore there is a clear correlation between identified contacts and the degree of overlap, but this information is not required to determine the appropriate settings for detection. Indeed, the difference in the degree of overlap between VGLUT1 objects determined to be synaptic contacts by the algorithm and those objects not classified as synaptic contacts is different enough (approximately 5-fold, see Figure 11B) that reasonably accurate estimations of the numbers of synaptic contacts could be made simply by using the overlap criterion together with an appropriate voxel overlap threshold. But this illustrates an advantage of the center distance approach over voxel counting alone, in that no previous empirical knowledge of the appropriate levels of overlap for a synaptic contact is required. Consequently, the center distance algorithm may be useful in some scenarios to provide initial estimations of appropriate overlap thresholds where voxel overlap or intersection strategies are to be employed as primary methods for determining synaptic contacts.

How broadly applicable is the center distance algorithm in determining synaptic contacts? In this study, pre-synaptic terminals were revealed using antibodies against VGLUT1, which is highly enriched in sensory afferent terminals and provides a fairly

uniform signal throughout the axon terminal (Alvarez et al., 2004; Todd et al., 2003). Antibodies against other neurotransmitter transporters, such as glycine transporter type 2 (GlyT2), and vesicular acetylcholine transporter (VAChT) also display uniform signal throughout the respective terminals and would likely be well suited for analysis (Arvidsson et al., 1997; Zeilhofer et al., 2005). Common synaptic markers that are concentrated in only a portion of the terminal, such as synaptotagmin-1 and synaptic vesicle glycoprotein 2 (SV2), may also be suitable for analysis with the algorithm, although the size of the resulting objects will underestimate the actual size of the pre-synaptic terminal (Betley et al., 2009). Post-synaptic markers were not tested in this study, but the algorithm could also be adapted to detect such markers, either solely or in combination with a pre-synaptic marker (Evers et al., 2005; Lin et al., 2000). For the case where only a post-synaptic marker is evaluated as an indication of a synaptic contact, the acceptable distance requirement would be altered to require the COM of the post-synaptic marker be found at a distance less than the diameter of the dendrite at that location. Initial analysis of a small number of test images by manual inspection would be advisable to determine the density of a particular input type, and to optimize detection criteria of the center distance algorithm using strategies similar to those outlined in Figures 11 and 12.

A growing number of neuronal tracing strategies may also be amenable to analysis with the center distance algorithm. Axons of pre-synaptic neurons may be labeled by genetic or viral means, or by direct dye injection. Varicosities that likely correspond to synaptic terminals can be segmented from the thinner axonal shafts during image pre-processing, although the final shape may be less uniform than for an antibody

labeled terminal (Wouterlood et al., 2007). Viral transfection of neurons with GFP or other fluorescent markers as well as genetic strategies such as Brainbow mice may allow quantification of inputs from several different neuronal types onto a single post-synaptic neuronal target (Livet et al., 2007; Stepien et al., 2010). While multi-channel fluorescent axons may represent a challenge during image pre-processing and segmentation (Lu et al., 2009), the center distance algorithm is expandable to accommodate any number of potential synaptic object channels for analysis.

It must be stressed that determination of synaptic contacts with light microscopy alone is not definitive. Some pre-synaptic terminals determined with our algorithm, or with other methods, may not make actual synaptic contact. Correlation with electron microscopy would be required for absolute determination. Such correlative analysis has been undertaken for determination of serotonergic contacts on motor neurons (Alvarez et al., 1998). Approximately 85% (18 of 21 terminals examined) of serotonergic contacts proposed by manual inspection at the light microscopic level were confirmed with electron microscopy. Thin glial processes occupied the space between terminals and dendrites in the negative cases. Serotonergic terminals may not require synaptic contact for modulation of nearby dendrites, but may also act through volume transmission in the spinal cord where these synapses were analyzed (Ridet et al., 1993). In this case, the center distance algorithm can be a valuable tool to objectively identify all synaptic terminals located within a certain distance from the dendrite, regardless of whether or not they satisfy the criterion for actual synaptic contact. Another study which analyzed a more limited number (n=3) of inhibitory terminals, confirmed with electron microscopy all of the contacts defined by light microscopy (Fyffe, 1991). Ratiometric criteria used in

light microscopy to determine if an axonal swelling represented a site of synaptic contact (diameter of swelling greater than twice that of the parent axon) have also been confirmed in a series of experiments to analyze labeled axons with electron microscopy (Rose et al., 1999). In summary, analysis by light microscopy likely returns a modest overestimate of synaptic connectivity, the extent of which may vary with the particular type of input studied. Nevertheless, strict application of objective criteria for contact detection, such as implemented here with the center distance algorithm, likely provides a reasonably accurate and stable estimate of synaptic connectivity. A significant advantage of automated contact determination is elimination of subjective judgment about contact validity arising from multiple users.

The additional feature of being able to account for potential shrinkage of the tissue along the z-axis is potentially advantageous, but is our method appropriate? Our adaptation to the analysis of the dendrite and potential contact data was to utilize linear extrapolation to determine a new Z position for each point of the centerline and the center of mass for the potential contacts. This is also based upon the assumption that the measurement is being made from the bottom of the tissue, closest to the plate, and as such most of the shrinkage would occur near the top of the tissue. The resulting change in location would then be relatively minimal near the bottom of the tissue and greatest at the top, hence the notion in using the linear extrapolation and having a fixed bottom point.

Unfortunately this adaptation has not been as successful as we had hoped. While it does eliminate some of the additional contacts the algorithm picks up without addressing for the z-axis shrinkage, it also rules out a few actual contacts when compared to the initial image from day 0. This is most likely because the shrinkage is not entirely

linear in nature and additionally compounded by several other changes due to the shrinkage and multiple imaging sessions. First off, it is hard to tell how the dendrite responds to this shrinkage. With basic compression in fixed tissue, there should be no relative decrease in the surface area of the dendrite. As such, the volume should have a minimal change, however this appears to not be the case (Table 6, Day 28). Changes in volume from day 0 to 7 and then to 14 are minimal. The major increase in volume at day 28 is rather confounding. It is quite possible that the fluorescence in the dendrite is becoming relatively equal and throwing off the active contouring Imaris uses to generate the isosurface. This could result in the increased volume that is observed as a result of a thresholding that encompasses a greater area due to the relatively small changes that can be detected in the fluorescence of the dendrite in an outward radial direction.

This is further compounded by the fact that there is evidence that potential contacts are being pushed into a position where the segmentation becomes an issue (Table 6 & Figure 13). Such physical movement of the VGLUT1 in the tissue sample can be a major issue when it comes to determining which ones are actual contacts, either by manual or automated analysis. VGLUT1 object counts decreased at each of the time points however when normalized by image volume. The day 28 VGLUT1 object number to image volume ratio increased when compared to day 14. It's hard to say what sort of implication this has as the average radius was still greater at day 28 compared to all of the other time points (Table 6 & Figure 14). Most likely it is a result of the thresholding by Imaris overestimating the volume of the VGLUT1 potential contacts in a similar fashion to the dendrite at the same time point and ultimately due to the photo-bleaching in the image. The movement of the VGLUT1 objects also poses an additional problem. The

potential contacts both move into an acceptable range to be determined as a contact and out of range of such detection (Figure 13, rows B, C & D). In fact, the potential contacts that are missing in the latter time points in Figure 13 row B are still there but are not determined to be actual objects by Imaris due to their size, fluorescence intensity or both.

So what do these results ultimately tell us in regards to the z-axis shrinkage issue? Ultimately it is of utmost importance to image the tissue sample as soon as possible after plating and cover slipping. In addition it is important to image everything that might be of interest due to the compounded effects of photo-bleaching and shrinkage along the z-axis.

Appendix A. Pseudocode outlining procedures to determine dendrite path and identify putative synaptic contacts in a single 3D image data set. Actual code is implemented in Matlab.

```
//Perimeter determination

FOR each voxel in the image
    IF voxel value equals 1 AND any 26-way connected neighbor voxel value equals 0
            // voxel is part of the perimeter and is added to Perimeter Matrix
END

// Step-wise centroid determination
FOR each position along the X dimension of the Perimeter Matrix
        Calculate mean position of all Y and Z positions equal to 1        //YZ Centroid
END
FOR each position along the Y dimension of the Perimeter Matrix
        Calculate mean position of all X and Z positions equal to 1        //XZ Centroid
END
FOR each position along the Z dimension of the Perimeter Matrix
        Calculate mean position of all X and Y positions equal to 1        //XY Centroid
END

Using Boolean OR logic, combine the three centroid matrices into one Centroid Matrix
```

Pseudocode outlining procedure for generating a continuous centerline for each dendritic segment in a single 3D image data set.

```
// Centerline determination
DISPLAY 2D projection (XY) of Centroid Matrix
GET graphical user input to indicate Start and Stop locations for centerline analysis
        // User must choose only (1) Start location, but can choose multiple Stop
        // locations in the image to account for branching of dendrite.
        // Primary axis of dendrite segments is based on the Start and Stop locations.
DETERMINE number of segments made up of 2 or more connected voxels in Centroid
        Matrix
CALCULATE mean number of connected voxels in each segment
        // Total number of voxels / number of segments
COPY segments longer than one-half of the mean segment length to matrix Centerline
        Segments
```

```
FOR the number of segments in Centerline Segments
        DETERMINE start and stop coordinates of each segment
END
SORT segments pairing end to start coordinates of separate segments
FOR one less than the number of segments in Centerline Segments
        IF segment end point is not equal to a user-defined Stop location
                CALL function GAP FILLING
                // This function connects end point of current segment to nearest start
                // point of another segment
END // Completed centerline is now continuous between user-defined Start and
         Stops

// GAP FILLING function
function: GAP FILLING
SET Current Position equal to Segment(n) end coordinate
WHILE Current Position is not equal to Segment(n+1) start coordinate
        SET Distance equal to distances between the 26-way connected voxels that
        neighbor the Current Position and the start voxel of Segment(n+1).  //Distance
        matrix contains X,Y,Z coordinate of neighbor as well as distance
        SET Sorted Distance equal to ascending distance values from Distance matrix
        mark Current Position with a 1
        INIT Invalid equal to 1
        INIT Iteration equal to 1
        WHILE Invalid equals 1
                FIND Index of Distance where distance equals Sorted Distance (Iteration)
                SET Next Position equal to X,Y,Z coordinates of Distance (Index)
                INCREMENT Iteration
                IF Next Position is outside bounds of the dendrite
                        Invalid = 1
                ELSE
                        Invalid = 0;
        END
        SET Current Position equal to Next Position
END
RETURN the connected matrix

// Determination of Path along the completed centerline from user-defined Start
// location to all Stop locations.
FOR the number of user-defined Stop locations
        INIT current position equal to user-defined Start location
        INIT Counter to 1
        INIT Movement Direction to "First Choice Direction"
        WHILE Current Position is not equal to Stop location
                // Using a hierarchy of cases from "First Choice Direction" to
                // "DEADEND"
```

```
            CASE "First Choice Direction"  // Based on status of Movement Direction
                SET New Position equal to next location based on current case
                    IF New Position is part of the unmarked center line AND
                    Movement Direction not equal to 'DEADEND'
                    SET Moves(Counter) = Current Position and next
                        movement direction in the hierarchy
                    // marks Current Position voxel as "visited"
                    INCREMENT Counter value by one
                ELSEIF Movement Direction = 'DEADEND'
                    SET Next Position to the position given by
                        Moves(Counter-1)
                    SET Movement Direction according to next movement
                        direction stored in Moves(Counter-1)
                    DECREMENT Counter value by one
                ELSE
                    SET Movement Direction to utilize next direction in
                        movement hierarchy
            END
        END
// Final mapping of path taken for this segment
        FOR x equal to one to the value of Counter
            SET voxel at location Moves(x) to a value of 1 in matrix Path
        END
END

// Path is a matrix of X, Y, Z coordinates corresponding to the segment's path
// This algorithm will add additional columns for distance and bin number to Path
matrix
SET Position1 equal to user-defined Start position
SET Bin Size = 5 //microns
FOR itr equal to the value of one to the size of Path
        SET Position2 equal to X, Y, Z coordinate of Path(itr)
        SET Path(itr) equal to distance in Path(itr – 1) plus results of following operation:
√[Position2(X) − Position1(X)]² + [Position2(Y) − Position1(Y)]² + [Position2(Z) − Position1(Z)]²

        SET Position1 equal to Position2
        SET Path(itr) equal to the ceiling rounded value of Path(itr) distance / Bin Size
END

// 3Dmat is a copy of the original binary dendrite volume matrix where all voxels
```

// **belonging to the dendrite are set to a value of 1, while all other voxels equal 0.**
DIVIDE 3Dmat by 2 //**All dendrite voxels now have a value of 0.5**
SET start = user-defined Start location
SET 3Dmat location at start point to 1
INIT Iteration to 1
WHILE the number of voxels in 3Dmat equal to 0.5 is greater than 0
    FOR each location in 3Dmat with a value equal to Iteration
        FOR each 26-way connected neighboring voxel equal to 0.5
            SET that voxel location in 3Dmat to value of (Iteration + 1)
    INCREMENT Iteration by one
END

// **Determination of dendrite radius for each bin in Path**
// **This algorithm will add a radius column to the Path matrix**
FOR itr equal to one to number of bins in the Path matrix
    SET Loc1 = first X,Y,Z location for bin number equal to itr in Path
    SET Loc2 = last X,Y,Z location for bin number equal to itr in Path
    SET Val1 = value of 3Dmat at Loc1
    SET Val2 = value of 3Dmat at Loc2
    FOR voxels with values less than val1 **OR** greater than val2
        SET those voxels in 3Dmat to zero
    IF number of objects remaining in 3Dmat is greater than one
        DELETE objects that do not contain points Loc1 **AND** Loc2
    SET Volume equal to the number of non-zero voxels remaining in 3Dmat
    SET Path radius where bin equals itr equal to $(Volume/(\pi * bin\ size))^{1/2}$
    // **Volume calculation can be adjusted to account for uneven voxel**
    // dimensions. i.e. Z-dimension is larger than XY dimensions.
END

// **Putative synaptic contact information is imported as Contact Info matrix**
// **Contact Info contains X,Y,Z location of center of mass (CoM) and the volume**
// **measurement for each putative contact object in image**
// **Determination of radius for putative contacts**
FOR each Contact
    SET Contact Info radius to value determined by following equation:
        $(3 * Volume/4 * \pi)^{1/3}$
END

// **Linking putative contacts to nearest location in Path**

// **May be repeated for unshared path information IE: after a bifurcation**
// **The variable Terminal contains the X,Y,Z location for the putative contact CoM**
INIT Current Shortest equal to 1
FOR each Terminal
    FOR itr equal to one to size of Path
        SET Dist(itr) =
$$\sqrt{[Path(X) - Terminal(X)]^2 + [Path(Y) - Terminal(Y)]^2 + [Path(Z) - Terminal(Z)]^2}$$
        IF itr equals 1 **OR** Dist(itr) is less than Dist(Current Shortest)
            SET Current Shortest equal to itr
    END
    SET Contact Info to store X, Y, Z location of Path(Current Shortest)
    // **x is a variable number for the % buffer the user wishes to allow**
    SET Acceptable Distance = Contact Info radius + Path(current shortest) radius ±
        x% * (Contact Info radius + Path(current shortest) radius)
    IF Dist(current shortest) is less than or equal to Acceptable Distance
        SET Terminal as Synapse
        SET Terminal as element of Neighborhood
    ELSEIF Dist(Current Shortest) is less than or equal to 5µm
        SET Terminal as element of Neighborhood
END
//**Matlab command line output is displayed, data passed to Imaris for visualization,**
// and tabular data regarding dendrite length and surface area, synaptic contact
// location and density saved in Excel format.

Appendix B. Sample file output for modeling in the .swc file format.

```
# ORIGINAL_SOURCE NeuronStudio 0.8.80
# CREATURE
# REGION
# FIELD/LAYER
# TYPE
# CONTRIBUTOR
# REFERENCE
# RAW
# EXTRAS
# SOMA_AREA
# SHINKAGE_CORRECTION 1.0 1.0 1.0
# VERSION_NUMBER 1.0
# VERSION_DATE 2007-07-24
# SCALE 1.0 1.0 1.0
1 3 1 961 77 0.71497 -1
2 3 2 961 77 0.71497 1
3 3 3 961 77 0.71497 2
4 3 4 961 77 0.71497 3
5 3 5 961 78 0.71497 4
6 3 6 961 78 0.71497 5
7 3 7 960 78 0.71497 6
8 3 8 960 78 0.71497 7
9 3 9 960 79 0.71497 8
10 3 10 960 78 0.71497 9
11 3 11 959 79 0.71497 10
12 3 12 959 79 0.71497 11
13 3 13 959 79 0.71497 12
14 3 14 959 79 0.71497 13
15 3 15 958 79 0.71497 14
16 3 16 958 79 0.71497 15
17 3 17 957 79 0.71497 16
18 3 18 957 80 0.71497 17
19 3 19 957 80 0.71497 18
.
.
.
1169 3 859 51 20 0.59727 1168
1170 3 860 50 20 0.59727 1169
1171 3 860 49 20 0.59727 1170
1172 3 861 48 20 0.59727 1171
1173 3 861 47 20 0.59727 1172
1174 3 861 46 20 0.59727 1173
1175 3 862 45 20 0.59727 1174
1176 3 862 44 20 0.59727 1175
1177 3 862 43 20 0.59727 1176
1178 3 862 42 20 0.59727 1177
1179 3 862 41 20 0.59727 1178
1180 3 862 40 21 0.59727 1179
1181 3 862 39 21 0.59727 1180
```

Appendix C. Location of on-line materials.

Neuron Studio: http://research.mssm.edu/cnic/tools-ns.html

Supplemental Videos: http://www.sciencedirect.com/science/article/pii/S0165027011003566

References

Alvarez FJ, Fyffe RE. The continuing case for the Renshaw cell. J Physiol, 2007; 584: 31-45.

Alvarez FJ, Pearson JC, Harrington D, Dewey D, Torbeck L, Fyffe RE. Distribution of 5-hydroxytryptamine-immunoreactive boutons on alpha-motoneurons in the lumbar spinal cord of adult cats. J Comp Neurol, 1998; 393: 69-83.

Alvarez FJ, Villalba RM, Zerda R, Schneider SP. Vesicular glutamate transporters in the spinal cord, with special reference to sensory primary afferent synapses. J Comp Neurol, 2004; 472: 257-80.

Arvidsson U, Riedl M, Elde R, Meister B. Vesicular acetylcholine transporter (VAChT) protein: a novel and unique marker for cholinergic neurons in the central and peripheral nervous systems. J Comp Neurol, 1997; 378: 454-67.

Ballou EW, Smith WB, Anelli R, Heckman CJ. Measuring dendritic distribution of membrane proteins. J Neurosci Methods, 2006; 156: 257-66.

Betley JN, Wright CV, Kawaguchi Y, Erdelyi F, Szabo G, Jessell TM, Kaltschmidt JA. Stringent specificity in the construction of a GABAergic presynaptic inhibitory circuit. Cell, 2009; 139: 161-74.

Bower JM, Beeman D. Constructing realistic neural simulations with GENESIS. Methods Mol Biol, 2007; 401: 103-25.

Brown AG, Fyffe RE. Direct observations on the contacts made between Ia afferent fibres and alpha-motoneurones in the cat's lumbosacral spinal cord. J Physiol, 1981; 313: 121-40.

Cannon RC, Turner DA, Pyapali GK, Wheal HV. An on-line archive of reconstructed hippocampal neurons. J Neurosci Methods, 1998; 84: 49-54.

Cho KO, Hunt CA, Kennedy MB. The rat brain postsynaptic density fraction contains a homolog of the Drosophila discs-large tumor suppressor protein. Neuron, 1992; 9: 929-42.

Wen Q, Chklovski DR. A cost-benefit analysis of neuronal morphology. J. Neurophysiol, 2008; 99: 2320-2328

Conradi S, Cullheim S, Gollvik L, Kellerth JO. Electron microscopic observations on the synaptic contacts of group Ia muscle spindle afferents in the cat lumbosacral spinal cord. Brain Res, 1983; 265: 31-9.

Conradi S, Skoglund S. Observations on the ultrastruture and distribution of neuronal and glial elements on the motoneuron surface in the lumbosacral spinal cord of the cat during postnatal development. Acta Physiol Scand Suppl, 1969; 333: 5-52.

Essrich C, Lorez M, Benson JA, Fritschy JM, Luscher B. Postsynaptic clustering of major GABAA receptor subtypes requires the gamma 2 subunit and gephyrin. Nat Neurosci, 1998; 1: 563-71.

Evers JF, Muench D, Duch C. Developmental relocation of presynaptic terminals along distinct types of dendritic filopodia. Dev Biol, 2006; 297: 214-27.

Evers JF, Schmitt S, Sibila M, Duch C. Progress in functional neuroanatomy: precise automatic geometric reconstruction of neuronal morphology from confocal image stacks. J Neurophysiol, 2005; 93: 2331-42.

Fyffe RE. Spinal motoneurons: synaptic inputs and receptor organization. In: Cope TC, editor. Motor neurobiology of the spinal cord. 2001; Boca Raton, FL: CRC Press. p 21–46.

Fyffe RE. Spatial distribution of recurrent inhibitory synapses on spinal motoneurons in the cat. J Neurophysiol, 1991; 65: 1134-49.

Gleeson P, Crook S, Cannon RC, Hines ML, Billings GO, Farinella M, Morse TM, Davison AP, Ray S, Bhalla US, Barnes SR, Dimitrova YD, Silver RA. NeuroML: a language for describing data driven models of neurons and networks with a high degree of biological detail. PLoS Comput Biol, 2010; 6: e1000815.

Grande G, Armstrong S, Neuber-Hess M, Rose PK. Distribution of contacts from vestibulospinal axons on the dendrites of splenius motoneurons. J Comp Neurol, 2005; 491: 339-51.

Grande G, Bui TV, Rose PK. Distribution of vestibulospinal contacts on the dendrites of ipsilateral splenius motoneurons: an anatomical substrate for push-pull interactions during vestibulocollic reflexes. Brain Res, 2010; 1333: 9-27.

Hausser M, Mel B. Dendrites: bug or feature? Curr Opin Neurobiol, 2003; 13: 372-83.

Hines ML, Carnevale NT. The NEURON simulation environment. Neural Comput, 1997; 9: 1179-209.

Hines ML, Morse T, Migliore M, Carnevale NT, Shepherd GM. ModelDB: A Database to Support Computational Neuroscience. J Comput Neurosci, 2004; 17: 7-11.

Jakobs TC, Koizumi A, Masland RH. The spatial distribution of glutamatergic inputs to dendrites of retinal ganglion cells. J Comp Neurol, 2008; 510: 221-36.

Jeon CJ, Kong JH, Strettoi E, Rockhill R, Stasheff SF, Masland RH. Pattern of synaptic excitation and inhibition upon direction-selective retinal ganglion cells. J Comp Neurol, 2002; 449: 195-205.

Kirsch J, Wolters I, Triller A, Betz H. Gephyrin antisense oligonucleotides prevent glycine receptor clustering in spinal neurons. Nature, 1993; 366: 745-8.

Koizumi A, Jakobs TC, Masland RH. Regular mosaic of synaptic contacts among three retinal neurons. J Comp Neurol, 2011; 519: 341-57.

Lin B, Martin PR, Grunert U. Expression and distribution of ionotropic glutamate receptor subunits on parasol ganglion cells in the primate retina. Vis Neurosci, 2002; 19: 453-65.

Lin B, Martin PR, Solomon SG, Grunert U. Distribution of glycine receptor subunits on primate retinal ganglion cells: a quantitative analysis. Eur J Neurosci, 2000; 12: 4155-70.

Livet J, Weissman TA, Kang H, Draft RW, Lu J, Bennis RA, Sanes JR, Lichtman JW. Transgenic strategies for combinatorial expression of fluorescent proteins in the nervous system. Nature, 2007; 450: 56-62.

Lu J, Fiala JC, Lichtman JW. Semi-automated reconstruction of neural processes from large numbers of fluorescence images. PLoS One, 2009; 4: e5655.

Mackie M, Hughes DI, Maxwell DJ, Tillakaratne NJ, Todd AJ. Distribution and colocalisation of glutamate decarboxylase isoforms in the rat spinal cord. Neuroscience, 2003; 119: 461-72.

Marrs GS, Green SH, Dailey ME. Rapid formation and remodeling of postsynaptic densities in developing dendrites. Nat Neurosci, 2001; 4: 1006-13.

Mears SC, Frank E. Formation of specific monosynaptic connections between muscle spindle afferents and motoneurons in the mouse. J Neurosci, 1997; 17: 3128-35.

Mehnert A, Jackway P. An improved seeded region growing algorithm. Pattern Recognition Letters, 1997; 18: 1064-71.

Meijering E. Neuron tracing in perspective. Cytometry A, 2010; 77: 693-704.

Meijering E, Jacob M, Sarria JC, Steiner P, Hirling H, Unser M. Design and validation of a tool for neurite tracing and analysis in fluorescence microscopy images. Cytometry A, 2004; 58: 167-76.

Meseke M, Evers JF, Duch C. Developmental changes in dendritic shape and synapse location tune single-neuron computations to changing behavioral functions. J Neurophysiol, 2009; 102: 41-58.

Miles GB, Hartley R, Todd AJ, Brownstone RM. Spinal cholinergic interneurons regulate the excitability of motoneurons during locomotion. Proc Natl Acad Sci U S A, 2007; 104: 2448-53.

Pierce JP, Mendell LM. Quantitative ultrastructure of Ia boutons in the ventral horn: scaling and positional relationships. J Neurosci, 1993; 13: 4748-63.

Redman S, Walmsley B. The time course of synaptic potentials evoked in cat spinal motoneurones at identified group Ia synapses. J Physiol, 1983; 343: 117-33.

Reese J, Zaranek S. GPU programming in Matlab. <http://www.mathworks.com/company/newsletters/articles/gpu-programming-in-matlab.html?s_cid=fb_wall_10-4-11_newsletter_gpu>, 2011

Ridet JL, Rajaofetra N, Teilhac JR, Geffard M, Privat A. Evidence for nonsynaptic serotonergic and noradrenergic innervation of the rat dorsal horn and possible involvement of neuron-glia interactions. Neuroscience, 1993; 52: 143-57.

Rodriguez A, Ehlenberger DB, Dickstein DL, Hof PR, Wearne SL. Automated three-dimensional detection and shape classification of dendritic spines from fluorescence microscopy images. PLoS One, 2008; 3: e1997.

Rodriguez A, Ehlenberger DB, Hof PR, Wearne SL. Rayburst sampling, an algorithm for automated three-dimensional shape analysis from laser scanning microscopy images. Nat Protoc, 2006; 1: 2152-61.

Rodriguez A, Ehlenberger DB, Hof PR, Wearne SL. Three-dimensional neuron tracing by voxel scooping. J Neurosci Methods, 2009; 184: 169-75.

Rose PK, Ely S, Norkum V, Neuber-Hess M. Projections from the lateral vestibular nucleus to the upper cervical spinal cord of the cat: A correlative light and electron microscopic study of axon terminals stained with PHA-L. J Comp Neurol, 1999; 410: 571-85.

Rose PK, Jones T, Nirula R, Corneil T. Innervation of motoneurons based on dendritic orientation. J Neurophysiol, 1995; 73: 1319-22.

Sato M, Bitter I, Bender MA, Kaufman AE, and Nakajima M. TEASAR: Tree-Structure Extraction Algorithm for Accurate and Robust Skeletons. Pacific Conf Comput Graph Appl, 2000; 281-289

Schmitt S, Evers JF, Duch C, Scholz M, Obermayer K. New methods for the computer-assisted 3-D reconstruction of neurons from confocal image stacks. Neuroimage, 2004; 23: 1283-98.

Stepien AE, Tripodi M, Arber S. Monosynaptic rabies virus reveals premotor network organization and synaptic specificity of cholinergic partition cells. Neuron, 2010; 68: 456-72.

Todd AJ, Hughes DI, Polgar E, Nagy GG, Mackie M, Ottersen OP, Maxwell DJ. The expression of vesicular glutamate transporters VGLUT1 and VGLUT2 in neurochemically defined axonal populations in the rat spinal cord with emphasis on the dorsal horn. Eur J Neurosci, 2003; 17: 13-27.

Vasilkoski Z, Stepanyants A. Detection of the optimal neuron traces in confocal microscopy images. J Neurosci Methods, 2009; 178: 197-204.

Wearne SL, Rodriguez A, Ehlenberger DB, Rocher AB, Henderson SC, Hof PR. New techniques for imaging, digitization and analysis of three-dimensional neural morphology on multiple scales. Neuroscience, 2005; 136: 661-80.

Wouterlood FG, Boekel AJ, Meijer GA, Belien JA. Computer-assisted estimation in the CNS of 3D multimarker 'overlap' or 'touch' at the level of individual nerve endings: a confocal laser scanning microscope application. J Neurosci Res, 2007; 85: 1215-28.

Xiong G, Zhou X, Degterev A, Ji L, Wong ST. Automated neurite labeling and analysis in fluorescence microscopy images. Cytometry A, 2006; 69: 494-505.

Xu Y, Vasudeva V, Vardi N, Sterling P, Freed MA. Different types of ganglion cell share a synaptic pattern. J Comp Neurol, 2008; 507: 1871-8.

Zagoraiou L, Akay T, Martin JF, Brownstone RM, Jessell TM, Miles GB. A cluster of cholinergic premotor interneurons modulates mouse locomotor activity. Neuron, 2009; 64: 645-62.

Zeilhofer HU, Studler B, Arabadzisz D, Schweizer C, Ahmadi S, Layh B, Bosl MR, Fritschy JM. Glycinergic neurons expressing enhanced green fluorescent protein in bacterial artificial chromosome transgenic mice. J Comp Neurol, 2005; 482: 123-41.